Adaptive Model-Based Classification of PolSAR Data

Dong Li, *Member, IEEE*, and Yunhua Zhang, *Member, IEEE*

***Abstract*— An adaptive classification is developed as a hybrid of the eigenvector-based and the model-based target decompositions for polarimetric synthetic aperture radar (PolSAR) data. The classification adopts the canonical scattering models that widely used in model-based decompositions to provide an improvement for the well-known H/α classification. First, a correspondence principle is adopted to adaptively identify the matched canonical models. The selected models are parallelly combined based on the scattering similarity for a fine depiction of the scattering mechanism then. Twelve classes are finally obtained, and each one carries a unique symbol to show a specific scattering. The classification does not depend on a particular data set, avoids the hard partitioning, and solves the obscures in H/α. Comparison on the real PolSAR data sets with H/α and the existing scattering similarity-based classification validates the better discrimination.**

***Index Terms*— Radar polarimetry, scattering model, scattering similarity, target decomposition, unsupervised classification.**

I. Introduction

POLARIZATION is an essential property of electromagnetic wave [1]–[4]. The polarization state of the wave will change when interacting with a target. By analyzing the polarization of the scattering wave, we can obtain the physical and geometrical information regarding the target, and this is the main task of the polarimetric synthetic aperture radar (PolSAR) [2]–[4].

Different from monopolarization radar data, each data cell in PolSAR is not a complex number but a matrix. PolSAR image processing is just dedicated to identify useful information from the matrix for target recognition and discrimination. There are many approaches to achieve this, among which the polarimetric target decomposition should be the most popular one. This idea was proposed by Huynen [5] in 1970. Since then a great deal of decompositions have been developed, such as the Huynen-type phenomenological dichotomies [5]–[8], the eigenvector-based decompositions [9]–[11], the model-based decompositions [12]–[20], and the coherent decompositions [21]–[23], just to name a few. The comprehensive review on the existing decomposition techniques can be found in [24]. Target decomposition provides a "quick look" of the components of the complex scattering by identifying the dominant/average scattering, or expanding the scattering on some canonical scattering models. By statistically incorporating the decompositions into some advanced schemes, the unsupervised scattering classifications can also be achieved [8], [9], [25]. The well-known entropy/alpha (H/α) is just such a classification based on eigenvector-based decomposition [10]. It can enable a classification independent of a particular data set [9], and has been widely used in the PolSAR field [26]–[31].

Another approach to extract information from the matrix is in terms of the scattering similarity. Unlike target decompositions, this approach characterizes the unknown complex scattering by parallelly checking the similarity between the scattering and the canonical scatterings. Yang *et al.* [32] first devised such a parameter to measure the similarity between two single scatterers. It was extended by Chen *et al.* [33] to evaluate the similarity between a mixed scatterer and a single scatterer. A random similarity was devised recently to further measure the similarity between two mixed scatterers [34]. The parameter not only covers Yang and Chen similarities by enabling a general scattering similarity measurement, but also provides a fast alternative to the entropy parameter in depiction of the scattering randomness. Based on the Chen similarity, Chen *et al.* [35] proposed an unsupervised PolSAR classification by characterizing complex scattering based on the combination of canonical scattering models so as to tackle with the assumption in H/α that there is always a dominant average in each cell.

Although it can avoid some semantic obscures in H/α, the Chen classification cannot enable the equivalent target discrimination as H/α and four classes of it will be disenabled forever if target deorientation is conducted beforehand. This paper is originally dedicated to enable an improvement to the Chen classification. It is interesting that the devised adaptive classification also provides an improvement for H/α as a hybrid of the eigenvector-based and model-based decompositions. The classification is founded on the nine widely used canonical scattering models. It adopts a correspondence principle to select the matched models and uses the random similarity to parallelly combine the selected models to achieve a fine depiction of the scattering mechanisms. A total of 12 classes

Manuscript received April 25, 2017; revised January 30, 2018; accepted June 2, 2018. Date of publication July 17, 2018; date of current version November 22, 2018. This work was supported in part by the National Natural Science Foundation of China under Grant 41401406 and in part by the Youth Innovation Promotion Association of Chinese Academy of Sciences under Grant 2014131. *(Corresponding author: Dong Li.)*

D. Li is with the Key Laboratory of Microwave Remote Sensing, National Space Science Center, Chinese Academy of Sciences, Beijing 100190, China (e-mail: lidong@mirslab.cn).

Y. Zhang is with the Key Laboratory of Microwave Remote Sensing, National Space Science Center, Chinese Academy of Sciences, Beijing 100190, China, and also with the School of Electronic, Electrical and Communication Engineering, University of Chinese Academy of Sciences, Beijing 10049, China (e-mail: zhangyunhua@mirslab.cn).

Color versions of one or more of the figures in this paper are available online at http://ieeexplore.ieee.org.

Digital Object Identifier 10.1109/TGRS.2018.2845944

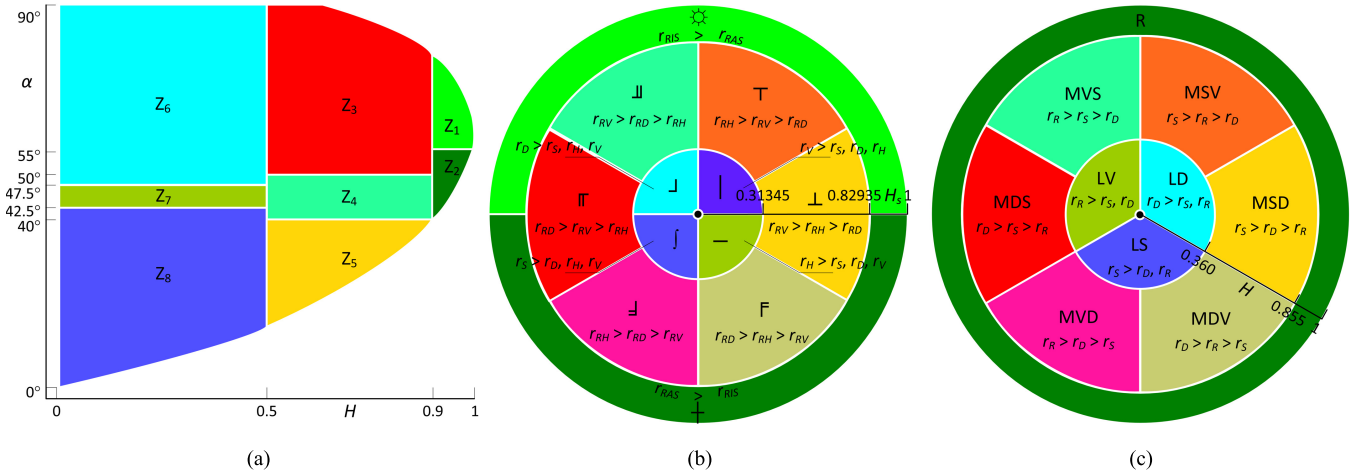

Fig. 1. Classification schemes of (a) H/α classification, (b) adaptive model-based classification, and (c) Chen classification.

are finally obtained with each class carrying a unique symbol to signify a specific scattering. Comparison with H/α and Chen classification validates the better discrimination.

The rest of this paper is arranged as follows. H/α is depicted in Section II. Section III presents the random similarity and the Chen classification. The adaptive classification is developed in Section IV and compared with H/α and Chen classification in Section V on real radar data set. Section VI further discusses the consistency and difference between the proposed classification and the model-based decomposition. This paper is concluded in Section VII with the formulation of the susceptibleness of Chen classification to deorientation being modeled in the Appendix.

II. Entropy/Alpha Classification

The Hermitian coherency matrix $\boldsymbol{T}$ of a polarimetric scatterer in monostatic backscattering is expressed as

$$\boldsymbol{T} = \begin{bmatrix} T_{11} & T_{12} & T_{13} \\ T_{21} & T_{22} & T_{23} \\ T_{31} & T_{32} & T_{33} \end{bmatrix}. \tag{1}$$

Following the eigenvalue-based Cloude decomposition, we can model a full-rank mixed scatterer $\boldsymbol{T}$ into the sum of three rank-1 single scatterers $\boldsymbol{T}_{Si}$ $(i = 1, 2, 3)$ [10]

$$\begin{cases} \boldsymbol{T} = \sum_{i=1}^{3} \boldsymbol{T}_{Si} = \sum_{i=1}^{3} \left(\boldsymbol{k}_{Si} \cdot \boldsymbol{k}_{Si}^{H}\right) \\ \text{with } \boldsymbol{k}_{Si} = \sqrt{\lambda_i}\boldsymbol{u}_i, \quad \lambda_1 \geq \lambda_2 \geq \lambda_3 \end{cases} \tag{2}$$

where superscript H denotes the conjugate transpose operation, and $\boldsymbol{k}_{Si}$ is the Pauli vector of $\boldsymbol{T}_{Si}$ which relates to the eigenvalues λ_i and eigenvectors $\boldsymbol{u}_i$ of $\boldsymbol{T}$. Decomposition (2) makes Cloude and Pottier [9] to propose a Bernoulli scattering model by treating $\boldsymbol{T}$ as single scattering $\boldsymbol{T}_{Si}$ occurring with probability proportional to λ_i. An entropy parameter H was then proposed to depict the scattering randomness by dividing scattering $\boldsymbol{T}$ into three states, the low entropy, medium entropy, and high entropy in terms of the boundaries $H = 0.5$ and $H = 0.9$. An angle α was raised to further characterize the scattering mechanism by classifying the three states into eight zones Z_i $(i = 1, 2, \ldots, 8)$ with boundaries $\alpha = 55°$ for Z_1 and Z_2, $\alpha = 50°$ for Z_3 and Z_4, $\alpha = 40°$ for Z_4 and Z_5, $\alpha = 47.5°$ for Z_6 and Z_7, and $\alpha = 42.5°$ for Z_7 and Z_8, as shown in Fig. 1(a). H/α has been widely used and it is one of the most successful methods to PolSAR data classification [2].

III. Random Similarity and Chen Classification

A. Random Similarity

The random similarity r between two mixed scatterers $\boldsymbol{T}$ and $\boldsymbol{T}_{\boldsymbol{c}}$ is defined as [34]

$$r(\boldsymbol{T}, \boldsymbol{T}_{\boldsymbol{c}}) = \frac{\mathrm{Tr}\left(\boldsymbol{T}\boldsymbol{T}_{\boldsymbol{c}}^{H}\right)}{\mathrm{Tr}(\boldsymbol{T})\mathrm{Tr}(\boldsymbol{T}_{\boldsymbol{c}})} \tag{3}$$

where Tr denotes the matrix trace. r possesses the properties of commutativity, traceless additivity, size and unitary invariance, and finite range [34]. It provides us a general similarity measure of any two scatterers. If $\boldsymbol{T}_{\boldsymbol{c}}$ is a single scatterer with $\boldsymbol{T}_{\boldsymbol{c}} = \boldsymbol{k}_{\boldsymbol{c}}\boldsymbol{k}_{\boldsymbol{c}}^{H}$, then (3) can be arranged as

$$r(\boldsymbol{T}, \boldsymbol{T}_{\boldsymbol{c}}) = \frac{\mathrm{Tr}\left(\boldsymbol{T}\boldsymbol{k}_{\boldsymbol{c}}\boldsymbol{k}_{\boldsymbol{c}}^{H}\right)}{\mathrm{Tr}(\boldsymbol{T})\mathrm{Tr}\left(\boldsymbol{k}_{\boldsymbol{c}}\boldsymbol{k}_{\boldsymbol{c}}^{H}\right)} = \frac{\boldsymbol{k}_{\boldsymbol{c}}^{H}\boldsymbol{T}\boldsymbol{k}_{\boldsymbol{c}}}{\mathrm{Tr}(\boldsymbol{T})\|\boldsymbol{k}_{\boldsymbol{c}}\|_2^2} \tag{4}$$

where $||\cdot||_2$ is the 2-norm, and r changes to Chen's parameter which measures the similarity between a mixed scatterer and a single scatterer [33]. Furthermore, if scatterer $\boldsymbol{T}$ is also a single scatterer and $\boldsymbol{T} = \boldsymbol{k}\boldsymbol{k}^{H}$, then (4) can be written as

$$r(\boldsymbol{T}, \boldsymbol{T}_{\boldsymbol{c}}) = \frac{\boldsymbol{k}_{\boldsymbol{c}}^{H}\boldsymbol{k}\boldsymbol{k}^{H}\boldsymbol{k}_{\boldsymbol{c}}}{\mathrm{Tr}(\boldsymbol{k}\boldsymbol{k}^{H})\|\boldsymbol{k}_{\boldsymbol{c}}\|_2^2} = \frac{|\boldsymbol{k}^{H}\boldsymbol{k}_{\boldsymbol{c}}|^2}{\|\boldsymbol{k}\|_2^2\|\boldsymbol{k}_{\boldsymbol{c}}\|_2^2}. \tag{5}$$

This is just Yang's parameter which measures the similarity of two single scatterers [32]. When $\boldsymbol{T}$ and $\boldsymbol{T}_{\boldsymbol{c}}$ in (3) correspond to the same scatterer, we obtain the self-similarity parameter r_{ss}

$$\begin{cases} r_{ss}(\boldsymbol{T}) = \dfrac{\mathrm{Tr}\left(\boldsymbol{T}\boldsymbol{T}^{H}\right)}{(\mathrm{Tr}(\boldsymbol{T}))^2} \\ \text{with } r_{ss} \in \left[\dfrac{1}{3} \quad 1\right]. \end{cases} \tag{6}$$

TABLE I

INVOLVED CANONICAL SCATTERING MODELS AND THEIR CORRESPONDING SCATTERING MECHANISMS, SCATTERING SIMILARITIES, AND SCATTERING ENTROPIES IN THE ADAPTIVE MODEL-BASED CLASSIFICATION AND THE CHEN CLASSIFICATION

Canonical Model	Scattering Mechanism	Scattering Similarity	Entropy	Involved Classification
$\boldsymbol{T_S}=\begin{bmatrix}1&0&0\\0&0&0\\0&0&0\end{bmatrix}$	Surface scattering	$r_S=\dfrac{T_{11}}{T_{11}+T_{22}+T_{33}}$	$H_s=0$	Chen classification Adaptive classification
$\boldsymbol{T_D}=\begin{bmatrix}0&0&0\\0&1&0\\0&0&0\end{bmatrix}$	Dihedral scattering	$r_D=\dfrac{T_{22}}{T_{11}+T_{22}+T_{33}}$	$H_s=0$	Chen classification Adaptive classification
$\boldsymbol{T_R}=\begin{bmatrix}0&0&0\\0&0&0\\0&0&1\end{bmatrix}$	45°-rotated dihedral scattering	$r_R=\dfrac{T_{33}}{T_{11}+T_{22}+T_{33}}$	$H_s=0$	Chen classification
$\boldsymbol{T_H}=\dfrac{1}{2}\begin{bmatrix}1&1&0\\1&1&0\\0&0&0\end{bmatrix}$	Horizontal dipole scattering	$r_H=\dfrac{T_{11}+T_{22}+2\mathrm{Re}(T_{12})}{2(T_{11}+T_{22}+T_{33})}$	$H_s=0$	Adaptive classification
$\boldsymbol{T_V}=\dfrac{1}{2}\begin{bmatrix}1&-1&0\\-1&1&0\\0&0&0\end{bmatrix}$	Vertical dipole scattering	$r_V=\dfrac{T_{11}+T_{22}-2\mathrm{Re}(T_{12})}{2(T_{11}+T_{22}+T_{33})}$	$H_s=0$	Adaptive classification
$\boldsymbol{T_{RD}}=\dfrac{1}{15}\begin{bmatrix}0&0&0\\0&8&0\\0&0&7\end{bmatrix}$	Random dihedral scattering	$r_{RD}=\dfrac{8T_{22}+7T_{33}}{15(T_{11}+T_{22}+T_{33})}$	$H_s=0.6269$	Adaptive classification
$\boldsymbol{T_{RH}}=\dfrac{1}{30}\begin{bmatrix}15&5&0\\5&7&0\\0&0&8\end{bmatrix}$	Random horizontal dipole scattering	$r_{RH}=\dfrac{15T_{11}+7T_{22}+8T_{33}+10\mathrm{Re}(T_{12})}{30(T_{11}+T_{22}+T_{33})}$	$H_s=0.7659$	Adaptive classification
$\boldsymbol{T_{RV}}=\dfrac{1}{30}\begin{bmatrix}15&-5&0\\-5&7&0\\0&0&8\end{bmatrix}$	Random vertical dipole scattering	$r_{RV}=\dfrac{15T_{11}+7T_{22}+8T_{33}-10\mathrm{Re}(T_{12})}{30(T_{11}+T_{22}+T_{33})}$	$H_s=0.7659$	Adaptive classification
$\boldsymbol{T_{RAS}}=\dfrac{1}{4}\begin{bmatrix}2&0&0\\0&1&0\\0&0&1\end{bmatrix}$	Random anisotropic scattering	$r_{RAS}=\dfrac{2T_{11}+T_{22}+T_{33}}{4(T_{11}+T_{22}+T_{33})}$	$H_s=0.8928$	Adaptive classification
$\boldsymbol{T_{RIS}}=\dfrac{1}{3}\begin{bmatrix}1&0&0\\0&1&0\\0&0&1\end{bmatrix}$	Random isotropic scattering	$r_{RIS}=\dfrac{1}{3}$	$H_s=1$	Adaptive classification

A scattering-similarity entropy H_s is then defined [36]

$$\begin{cases} H_s=-\log_3 r_{ss} \\ \text{with } H_s\in[0\quad 1]. \end{cases} \tag{7}$$

H_s is 0 for a single scatterer, is 1 for a depolarized scatterer, and is within 0–1 for a partially polarized scatterer. An analytical comparison of H_s and H is presented in [36] by formulating the rigorous H_s-H relationship, and it is shown that H_s is a competent alternative to H in description of the scattering randomness. Moreover, unlike the calculation of H which needs to conduct eigendecomposition pixelwisely on the whole PolSAR imagery, the calculation of H_s simply relates to the trace and the squared Frobenius norm $\mathrm{Tr}(\boldsymbol{T}\boldsymbol{T}^H)$ of $\boldsymbol{T}$, and it is thus very efficient [36].

B. Chen Classification

Different from Cloude–Pottier statistical interpretation, Chen *et al.* [35] gave another interpretation to (2). They also ascribed the mixed scattering $\boldsymbol{T}$ to three states but with the boundaries $H=0.36$ and $H=0.855$, and ranked the single scatterings $\boldsymbol{u}_i$ as the major scattering $\boldsymbol{u}_1$, the minor scattering $\boldsymbol{u}_2$, and the least scattering $\boldsymbol{u}_3$ based on λ_i. Then, they described the low-entropy state only with $\boldsymbol{u}_1$, represented the medium-entropy state with both $\boldsymbol{u}_1$ and $\boldsymbol{u}_2$, and depicted the high-entropy state with all $\boldsymbol{u}_1$, $\boldsymbol{u}_2$, and $\boldsymbol{u}_3$. Since eigenvectors $\boldsymbol{u}_i$ cannot provide a description of scattering mechanism independent of $\boldsymbol{T}$, Chen *et al.* [35] further used the canonical scattering models instead. As shown in Table I, the involved models are the surface scattering $\boldsymbol{T_S}$, the dihedral scattering $\boldsymbol{T_D}$, and the 45° rotated dihedral scattering $\boldsymbol{T_R}$. $\boldsymbol{T_R}$ is used to model the volume scattering and accounts for the cross-polarized HV scattering. Chen *et al.* [35] ranked them with the similarity parameters r_S, r_D, and r_R, which denote the similarities $r(\boldsymbol{T},\boldsymbol{T_S})$, $r(\boldsymbol{T},\boldsymbol{T_D})$, and $r(\boldsymbol{T},\boldsymbol{T_R})$, respectively, as listed in Table I. Among $\boldsymbol{T_S}$, $\boldsymbol{T_D}$, and $\boldsymbol{T_R}$, the one which produces the maximum similarity is treated as the major scattering, the minor similarity as the minor scattering, and the minimum similarity as the least scattering. In the state of low entropy, only the major scattering is considered and we obtain three classes, i.e., LS, LD, and LV. LD means low-entropy dihedral scattering and is identified when $r_D>r_S, r_R$. LS and LV can be analogously defined. Both major and minor scatterings are involved in the medium entropy, and six classes are then obtained which are MSD, MSV, MDS, MDV, MVS, and MVD. MSV denotes the medium-entropy surface–volume scattering which is attained when $r_S>r_R>r_D$. The other five classes can be likewise inferred. As for the high entropy, Chen *et al.* [35] wholly deemed it as one intact class R with the assumption that the contributions of all scattering mechanisms are nearly close here. Hence, scattering $\boldsymbol{T}$ is classified into a total of ten different classes.

C. Sufficiency and Deficiency of Chen Classification

The sufficiency of Chen classification rests in its disposal of the state of medium entropy. Angle α in H/α is extracted from the scattering $\boldsymbol{u}_0$ which is the statistical mean of scatterings $\boldsymbol{u}_i$ [9]. This indicates that α may only enable an average

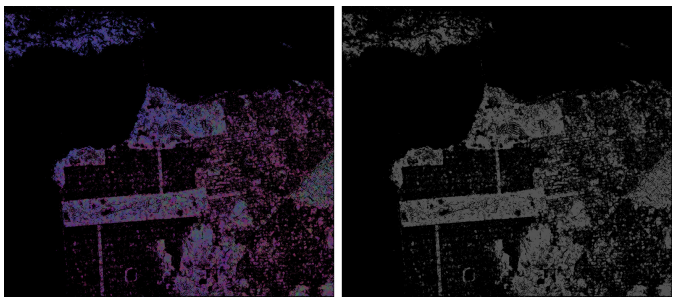

(a) (b)

Fig. 2. Illustrating the deficiency of Chen classification in the disposal of high-entropy state on the AIRSAR San Francisco scene. (a) RGB image of the high-entropy state. The image should present like the (b) gray image with low hue and saturation if follow Chen's assumption. However, the colors in (a) clearly reveal a different truth. Since we focus only on the high-entropy state here, the pixels attributed to low- and medium-entropy states are rendered as pure black.

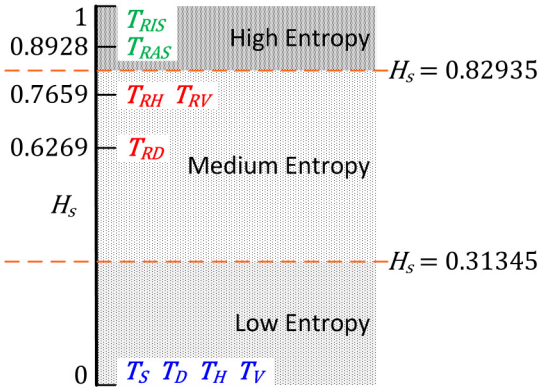

Fig. 3. Determination of the three random scattering states in the model-based classification by adaptively selecting the matched canonical scattering models in terms of a correspondence principle.

depiction of the scattering mechanism. Take Z_4 for example, it represents medium-entropy vegetation scattering with $\alpha \approx 45°$. However, Chen *et al.* [35] observed that the majority of Z_4 appears in MSD and MDS that denote dominant surface and dihedral scatterings instead. It is known that $\alpha > 45°$ for dihedral scattering and $\alpha < 45°$ for surface scattering, the weighted average α in MSD and MDS then approaches to 45° because the weights r_S and r_D are comparable [35]. This misleads H/α to identify MSD and MDS as Z_4. The combination of major scattering and minor scattering can thus avoid the obscure of mean scattering $\boldsymbol{u}_0$ in description of the scattering mechanism.

Chen *et al.* [35] modeled the volume scattering as a simple rotated dihedral scattering. However, volume scattering usually arises from the depolarization of odd- or even-bounce scatterings and is often modeled as a mixed scattering instead [12]–[20]. Chen *et al.* [35] have not evaluated the impact of target orientation on their classification. The same scatterer can be presented differently by a simple rotation about the line of sight (LOS) [37], [38]. As the result, a building may be identified as forest because orientation increases the cross-polarized scattering [39]–[41]. To avoid the influences, deorientation operator should be conducted first. As deducing in the Appendix, the T_{33} entry of $\boldsymbol{T}$ will be no larger than T_{22} after doing deorientation to minimize the cross-polarization. As a result, r_R will also be no larger than r_D and the four classes LV, MSV, MVS, and MVD will be disabled forever. This greatly influences the performance of the classification in medium- and low-entropy states.

In H/α, Cloude and Pottier [9] gave a dichotomy to high-entropy state based on the scattering mechanism. In the Chen classification, however, the high entropy is intactly kept as one class because all the scattering mechanisms are assumed to contribute equally here [35]. As for the involved canonical models $\boldsymbol{T_S}$, $\boldsymbol{T_D}$, and $\boldsymbol{T_R}$, this may signify that the similarity parameters r_S, r_D, and r_R are comparable when H of scattering $\boldsymbol{T}$ is high. To validate this, we construct an RGB image of the high entropy by assigning r_D, r_R, and r_S to the red, green, and blue, respectively. Fig. 2(a) shows the obtained image on NASA/JPL L-band AIRSAR data of San Francisco. The image should present like the gray image in Fig. 2(b) with very low hue if following Chen's assumption, because the three color components are comparable. However, the wide distributions of red, blue, and even green in Fig. 2(a) reveal a different truth: one can still tell different scattering mechanisms in high entropy. The disposal of high-entropy state in H/α is thus preferable.

IV. Adaptive Model-Based Classification

The adaptive mode-based classification is devised to remedy the aforementioned deficiencies to improve the performance of Chen classification and to enable a novel understanding of H/α from the model-based point of view.

Like the classifications of H/α and Chen, in the first step, we also divide scattering $\boldsymbol{T}$ into three states. As for their boundary, Cloude and Pottier [9] used $H = 0.5$ and $H = 0.9$, but Chen *et al.* [35] used $H = 0.36$ and $H = 0.855$. The former is set based on the general properties of the typical scatterings and has been validated on plenty of data sets [2], and the latter is obtained by statistically analyzing the scattering feature of AIRSAR data of San Francisco and should be adjusted according to application demand [35]. Instead of entropy H, we determine the states with entropy H_s since it is a fast and competent alternative to H [36].

Here, we adopt Chen's proposition to use canonical models in PolSAR classification. Nevertheless, unlike the Chen classification in which only the three canonical scattering models $\boldsymbol{T_S}$, $\boldsymbol{T_D}$, and $\boldsymbol{T_R}$ are considered and they are used to determine the scattering mechanism only, the proposed classification tries to use a total of nine canonical scattering models for a joint characterization of both the scattering mechanism and randomness. Table I lists the involved models, among which $\boldsymbol{T_S}$ and $\boldsymbol{T_D}$ are reserved, but $\boldsymbol{T_R}$ is removed due to its susceptibleness to orientation. Seven other models are added which are widely adopted in the model-based decompositions [12]–[20]. Table I also lists entropy H_s of each model, based on which we coarsely attribute these models into three categories, as displayed in Fig. 3. $\boldsymbol{T_S}$, $\boldsymbol{T_D}$, $\boldsymbol{T_H}$, and $\boldsymbol{T_V}$ belong to the first category with the low entropy $H_s = 0$. Here, $\boldsymbol{T_H}$ and $\boldsymbol{T_V}$ denote

the horizontal and vertical dipole scatterings, respectively, and they often serve as the origin of some volume scattering models such as $\boldsymbol{T_{RH}}$ and $\boldsymbol{T_{RV}}$. $\boldsymbol{T_{RH}}$ and $\boldsymbol{T_{RV}}$ represent a random version of $\boldsymbol{T_H}$ or $\boldsymbol{T_V}$ scatterers with nonuniform sine distribution for the orientation. They are dedicated to model the dominantly horizontal or vertical structures and constitute one of the important characters of the four-component model-based decompositions [13]–[15]. The second category is comprised of $\boldsymbol{T_{RH}}$, $\boldsymbol{T_{RV}}$, and a third model $\boldsymbol{T_{RD}}$ with the medium entropies $H_s = 0.7659$ and $H_s = 0.6269$. $\boldsymbol{T_{RD}}$ is a deoriented version of the Sato *et al.*'s [14] extended volume scattering to model a cloud of scatterer $\boldsymbol{T_D}$ with orientation also subjected to sine distribution. As an extension of $\boldsymbol{T_D}$, $\boldsymbol{T_{RD}}$ is competent to characterize the random volume scattering created by even-bounce structures. The third category contains the high-entropy canonical models $\boldsymbol{T_{RIS}}$ and $\boldsymbol{T_{RAS}}$ with entropies $H_s = 1$ and $H_s = 0.8928$. $\boldsymbol{T_{RIS}}$ shows the random isotropic scattering with the highest H_s. It has been adopted by An *et al.* [16] as an empirical model in their model-based decomposition. Like $\boldsymbol{T_{RH}}$ and $\boldsymbol{T_{RV}}$, $\boldsymbol{T_{RAS}}$ is also a random version of $\boldsymbol{T_H}$ or $\boldsymbol{T_V}$ but with uniform distribution for the dipole cloud orientation. It denotes the random anisotropic scattering. This model was employed by Cloude and Pottier [9] to characterize mixed scattering from highly anisotropic particles. Freeman and Durden [12] further used it in the three-component model-based decomposition for volume scattering from a forest canopy.

Based on these canonical scattering models, we then adopt a correspondence principle by describing scattering $\boldsymbol{T}$ only with models of the same state, and miscorrespondence is prohibited. As for scattering $\boldsymbol{T}$ with entropy H_s, this principle enables us an adaptive selection of the canonical models

$$\begin{cases} |H_s - 0| \le |H_s - 0.6269| & \rightarrow \boldsymbol{T_S}, \boldsymbol{T_D}, \boldsymbol{T_H}, \boldsymbol{T_V} \\ |H_s - 0.8928| < |H_s - 0.7659| & \rightarrow \boldsymbol{T_{RAS}}, \boldsymbol{T_{RIS}} \\ \text{else} & \rightarrow \boldsymbol{T_{RH}}, \boldsymbol{T_{RV}}, \boldsymbol{T_{RD}}. \end{cases} \tag{8}$$

Equation (8) can be easily solved

$$\begin{cases} 0 \le H_s \le 0.31345 & \rightarrow \boldsymbol{T_S}, \boldsymbol{T_D}, \boldsymbol{T_H}, \boldsymbol{T_V} \\ 0.31345 < H_s \le 0.82935 & \rightarrow \boldsymbol{T_{RH}}, \boldsymbol{T_{RV}}, \boldsymbol{T_{RD}} \\ 0.82935 < H_s \le 1 & \rightarrow \boldsymbol{T_{RAS}}, \boldsymbol{T_{RIS}}. \end{cases} \tag{9}$$

This indicates that we adopt $H_s = 0.31345$ and $H_s = 0.82935$ as the boundaries of the three states of randomness, as shown in Fig. 3. The boundaries are determined by the canonical models, thus do not depend on a particular data set.

The second step is dedicated to give a deep discrimination of the scattering mechanism based on random similarity. As for $\boldsymbol{T}$ in low-entropy state, canonical models $\boldsymbol{T_S}$, $\boldsymbol{T_D}$, $\boldsymbol{T_H}$, and $\boldsymbol{T_V}$ are matched to calculate the similarity parameters r_S, r_D, r_H, and r_V, respectively, as shown in Table I. Only the dominant similarity is revered in this state and four classes are obtained in terms of the combination and permutation (C_4^1) of r_S, r_D, r_H, and r_V. For convenient understanding, we denote each class with a symbol. As given in Fig. 1(b), $\int$ signifies the dominant surface scattering which is achieved when $r_S > r_D$, r_H, r_V. ⌋ denotes the dominant dihedral scattering which is ruled by $r_D > r_S$, r_H, r_V. — or | represents the dominant horizontal or vertical scattering which is determined when r_H or r_V is the maximum. Models $\boldsymbol{T_{RH}}$, $\boldsymbol{T_{RV}}$, and $\boldsymbol{T_{RD}}$ are matched to $\boldsymbol{T}$ of medium entropy, and similarities r_{RH}, r_{RV}, and r_{RD} are obtained accordingly, as shown in Table I. The minor similarity is also revered in this state, and six classes are then achieved in terms of the combination and permutation (C_3^2) of r_{RH}, r_{RV}, and r_{RD}. We also assign a symbol to each class but based on the pairwise combination of —, |, and ⌋. As given in Fig. 1(b), ⊤ symbolizes — above | which represents $r_{RH} > r_{RV} > r_{RD}$, i.e., the major horizontal scattering and minor vertical scattering, and its rotation ⊥ signifies $r_{RV} > r_{RH} > r_{RD}$. ⫤ denotes — above ⌋ which indicates $r_{RH} > r_{RD} > r_{RV}$, and its rotation ⊢ denotes $r_{RD} > r_{RH} > r_{RV}$. ⫦ implies | before ⌋ which signifies $r_{RV} > r_{RD} > r_{RH}$, and its rotation ⫪ reflects $r_{RD} > r_{RV} > r_{RH}$. $\boldsymbol{T_{RIS}}$ and $\boldsymbol{T_{RAS}}$ are identified for $\boldsymbol{T}$ of high entropy to compute the similarity parameters r_{RIS} and r_{RAS} listed in Table I. Only the dominant scattering is revered in this state and two classes (C_2^1) are attained, as shown in Fig. 1(b). As for $r_{RAS} > r_{RIS}$, the random anisotropic scattering is preferable and symbol ┼ is used. $\boldsymbol{T}$ approaches to a pure depolarizer when $r_{RIS} > r_{RAS}$, and the random isotropic scattering is obtained. We symbolize this class as ☼ (the sun) since sunlight is often fully depolarized [42]. A total of 12 classes are thus obtained.

For illustrating conveniently, we devise the circle in Fig. 1(b). The circle is comprised of three shells and 12 sectors. Each shell indicates a state of randomness with the depth depending on the state boundary, and transition among the shells signifies the increase (outward) or decrease (inward) of entropy H_s. Each sector locates in a specific state with a unique symbol denoting a particular scattering mechanism. Such circle can also be used to illustrate the scheme of Chen classification, as shown in Fig. 1(c). The developed classification is validated in the following.

V. Experiments and Analysis

Fig. 4(b) shows the classification of the widely used AIRSAR San Francisco data. Before classification, the refined Lee filter with 7×7 aligned window (denoted by RLF_7, and the meaning of RLF_n can be likewise inferred) is first used to suppress the speckle, and the deorientation operator is then performed. The typical scatterers such as ocean, building, bridge, forest, avenue, park, polo field, golf course, beach, island, and mountains are all well identified by the developed approach. The comparisons with H/α and Chen classification are conducted as follows.

A. Comparison With Entropy/Alpha

The H/α classification of San Francisco data is shown in Fig. 4(a). By rendering each pixel also with its allotted class color in Fig. 4(a), Fig. 5(a) displays the mapping of the classification in the H/α space. Our intuitive impression of Fig. 4(a) and (b) is their nice consistency but distinct difference. To illustrate these qualitatively and quantitatively, the classification in Fig. 4(b) is also mapped to the H/α space

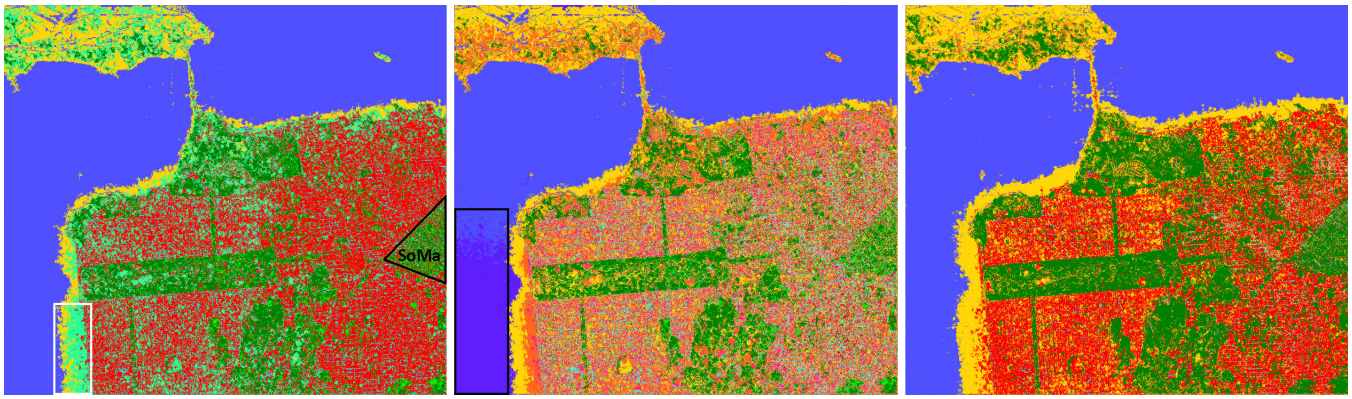

Fig. 4. Classification results of (a) H/α classification, (b) adaptive model-based classification (with deorientation), and (c) Chen classification (without deorientation) on the AIRSAR San Francisco data set. Each class in the three classifications is coded with the color assigned in Fig. 1.

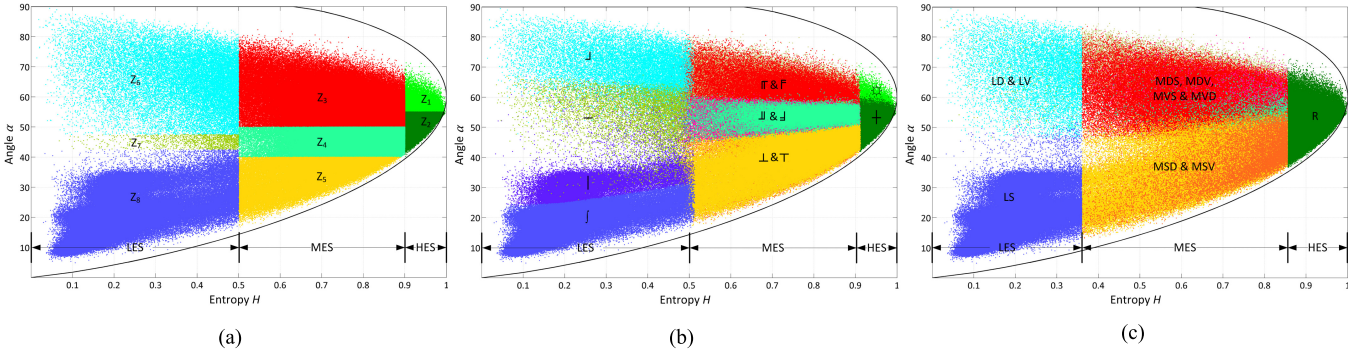

Fig. 5. Illustrating (a) H/α classification, (b) adaptive model-based classification (with deorientation), and (c) Chen classification (without deorientation) by mapping the classification results in Fig. 4 to the 2-D H/α space and coding each class also with the color assigned in Fig. 1. The abbreviations LES, MES, and HES denote the low-entropy state, the medium-entropy state, and the high-entropy state, respectively.

in Fig. 5(b). A confusion matrix is further produced in Table II with each row listing how many pixels of each class of the proposed approach being classified to the different zones of H/α. Two interesting results are obtained.

First, the two vertical borders among the three states are clear and straight in Fig. 5(b), and are just close to the Cloude–Pottier borders $H = 0.5$ and $H = 0.9$. From Table II, we also obtain the confusion matrix among the states of the two classifications

$$\boldsymbol{C} = \begin{bmatrix} 97.0603\% & 2.9397\% & 0 \\ 1.4835\% & 97.6444\% & 0.8721\% \\ 0 & 0.1835\% & 99.8165\% \end{bmatrix} \quad (10)$$

where the three rows of $\boldsymbol{C}$ denote how many pixels of the high-, medium-, and low-entropy states of the developed approach are registered to different states of H/α, respectively. As shown, the diagonal elements 97.06%, 97.64%, and 99.82% indicate the perfect consistency of the two classifications on three states. Thus, entropy H_s and the related boundaries are nice alternative to entropy H and the Cloude–Pottier boundaries in depiction of the randomness and in determination of the states, respectively.

In [36], a similarity-based H_s/α_s classification is proposed in terms of two parameters, i.e., the similarity-based angle α_s and entropy H_s by referring to the H/α classification. $H_s = 0.3092$ and $H_s = 0.8203$ are identified as the optimal approximation to the boundaries $H = 0.5$ and $H = 0.9$, which are determined by iteratively minimizing the misclassification between H_s/α_s and H/α on some typical PolSAR data sets. It is interesting that the boundaries (9) are pretty close to these optimal boundaries, and this is the underlying mechanism that supports the consistency between the proposed classification and H/α on the three states. Cloude and Pottier [9] indicated that the boundaries in H/α are not dependent on a particular data set although there is some degree of arbitrariness on setting them. The above consistency also validates such independent character of H boundaries because their alternative boundaries (9) are determined by the canonical models instead of by a particular data set.

Second, the 12 classes of the developed approach present the consistent pattern as the nine zones of H/α, as shown in Fig. 5(a) and (b). Take the medium-entropy state as an example, such as Z_3, Z_4, and Z_5, the six classes ⊤, ⊥, ⫤, ⫪, ⫫, and ⫯ also geometrically partition this state into three zones with clear borders, i.e., the upper zone ⫯ and ⫪, the middle zone ⫫ and ⫤, and the lower zone ⊥ and ⊤. H/α accomplishes Z_3, Z_4, and Z_5 using the hard thresholds $\alpha = 40°$ and $\alpha = 50°$. But the six classes in the proposed

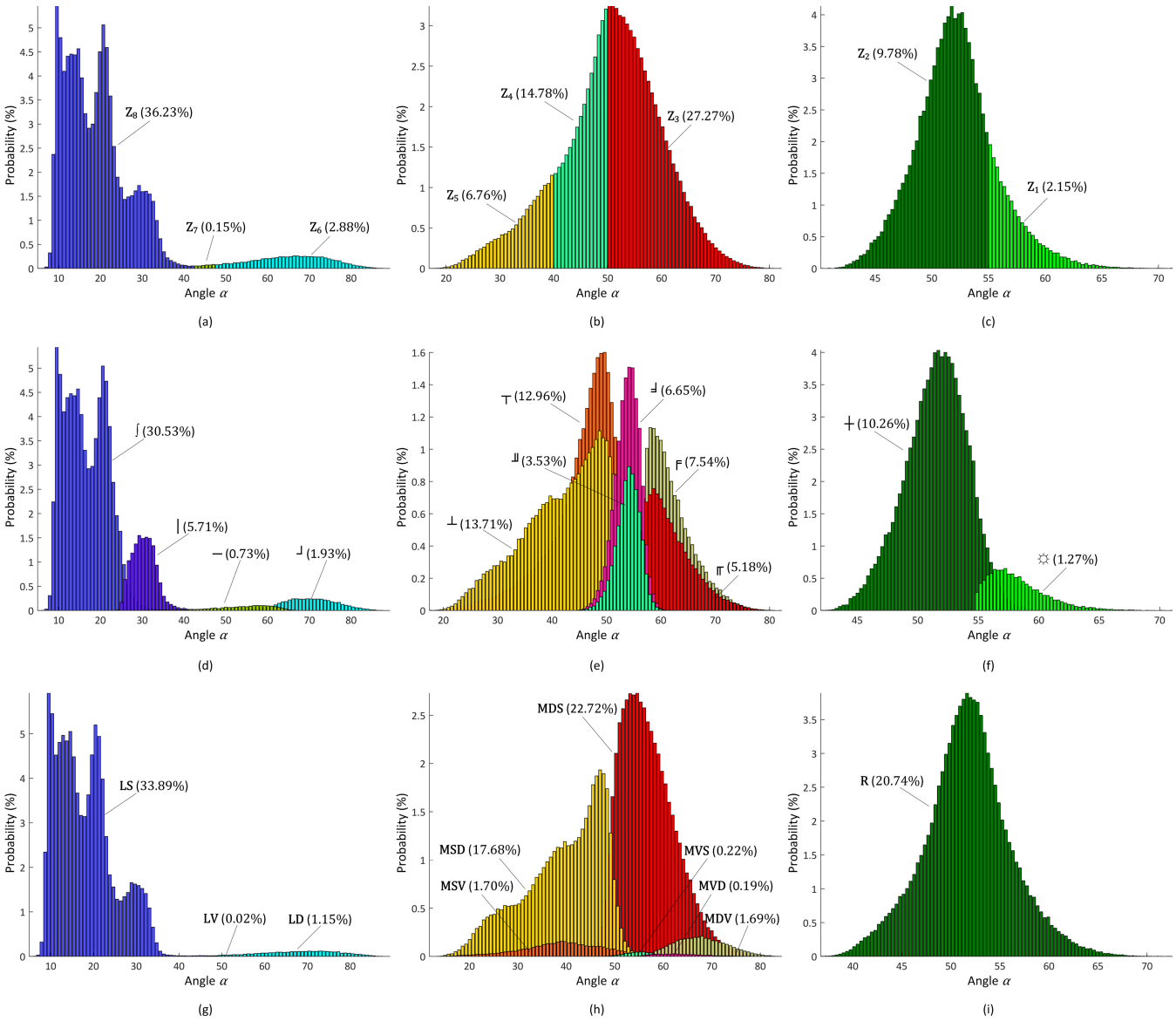

Fig. 6. Alpha angle histograms of (First row) H/α classification, (Second row) adaptive model-based classification (with deorientation), and (Third row) Chen classification (without deorientation) in (First column) low-entropy state, (Second column) medium-entropy state, and (Third column) high-entropy state on the AIRSAR San Francisco scene. The percentage in the bracket lists how many pixels of the scene are classified into a certain class.

approach are determined by the adaptive combination and permutation of canonical scattering models. It is interesting that such adaptive ruling can also enable a kind of thresholding. Nonetheless, the thresholding here is not hard but soft, as illustrated in Fig. 6 in terms of the angle α histogram of each class of the two classifications on San Francisco data. Park and Moon [30] showed that the arbitrarily fixed zone boundaries in H/α could result in noisy classification, and they used fuzzy logic to soften the boundaries to improve the classification. The proposed approach naturally enables such thresholding; thus, good results can be expected.

Although bearing the same number of zones, the coverage of the three medium-entropy zones in Fig. 6(b) differs from that in Fig. 6(e). As shown, the majority of the upper zone ⫪ and ⫪ and the middle zone ⫫ and ⫫ are covered by Z_3. As also reflected in Table II, 98.08%, 98.08%, 93.10%, and 93.24% of the pixels that classified to the classes ⫪, ⫪, ⫫, and ⫫ are registered to Z_3. Dihedral scattering ⫫ or ⫫ is contained in all the four classes ⫪, ⫪, ⫫, and ⫫, and the parallel addition of a second scattering — or ⫫ boosts the entropy of scattering process. This is consistent with the character of Z_3 in H/α, i.e., to account for the dihedral scattering with moderate entropy scattered from urban areas [9]. Thus, Z_3 is classified into four classes in the proposed approach, and better urban classification is shown in Fig. 4(b) than in Fig. 4(a). Moreover, we can also observe from Fig. 6(b) and (e) that the majority of Z_4 and Z_5 are covered in the lower zone ⫫ and ⫫. It is recorded in Table II that 59.51% of ⫫ and 47.14% of ⫫ are registered to Z_4, and there are also 33.96% of ⫫ and 15.89% of ⫫ classified to Z_5. Hence, classes ⫫ and ⫫ enable an alternative to Z_4 and Z_5. The white rectangle in Fig. 4(a) frames a beach area, the majority of which are classified into Z_4, the medium-entropy vegetation scattering. However, Chen *et al.* [35] indicated that beach

TABLE II

CONFUSION MATRIX BETWEEN THE ADAPTIVE MODEL-BASED CLASSIFICATION AND THE ENTROPY/ALPHA CLASSIFICATION ON THE AIRSAR SAN FRANCISCO DATA

Items		Cloude-Pottier H/α Classification							
		Z_1	Z_2	Z_3	Z_4	Z_5	Z_6	Z_7	Z_8
Adaptive Model-Based Classification	☼	97.48%	1.96%	0.56%	0	0	0	0	0
	┼	7.59%	89.18%	2.35%	0.88%	0	0	0	0
	╨	0.53%	1.21%	93.10%	4.60%	0	0.52%	0.04%	0
	╥	0.93%	0.01%	98.08%	0	0	0.98%	0	0
	╡	0.24%	0.42%	93.24%	5.25%	0	0.78%	0.07%	0
	╞	0.62%	0.01%	98.08%	0	0	1.29%	0	0
	┬	0	1.73%	22.61%	59.51%	15.89%	0.02%	0.07%	0.17%
	┴	0	2.26%	15.37%	47.14%	33.96%	0.01%	0.05%	1.21%
	┘	0	0	0.89%	0	0	99.09%	0.02%	0
	─	0	0	0.35%	0.16%	0.09%	80.67%	10.46%	8.27%
	│	0	0	0.02%	0.05%	0.13%	2.63%	0.88%	96.29%
	∫	0	0	0	0	0.12%	0	0.02%	99.86%

Each row of the matrix lists how many pixels of each class (in percent) of the adaptive model-based classification are classified into the different zones of H/α.

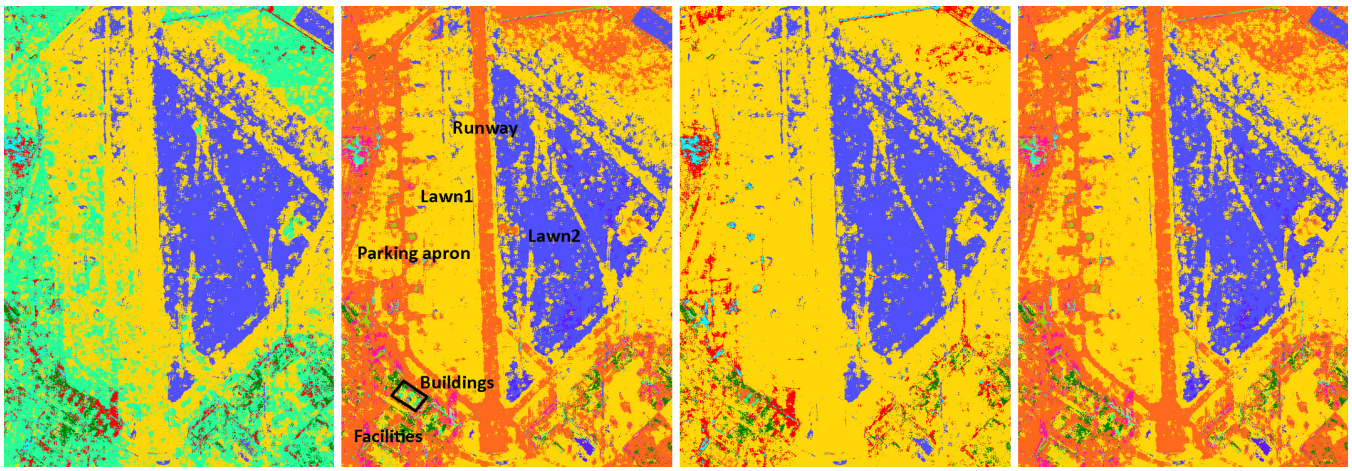

(a) (b) (c) (d)

Fig. 7. Classification results of (a) H/α classification, proposed adaptive model-based classifications (b) with and (d) without deorientation, and (c) Chen classification (without deorientation, because four of the ten classes in Chen classification will disappear after deorientation) on the ESAR Oberpfaffenhofen data. The coded color of each class in the three classifications is displayed in Fig. 1. Since Chen's statistical method cannot appropriately delimit the state borders on this data set, the H/α borders $H = 0.5$ and $H = 0.9$ are adopted in the Chen classification.

generally comprises of sand not vegetation, and they classified this area as MSD which denotes the major surface and minor dihedral scatterings, as exhibited in Fig. 4(c). In the proposed classification displayed in Fig. 4(b), the area is further classified into two parts ⊥ and ⊤. Such result is consistent with the Wishart $SPAN/H/A/\alpha$ classification proposed in [31]. The combination of ⊥ and ⊤, thus, behaves better than Z_4. Furthermore, Fig. 7 displays the classifications on DLR L-band ESAR data of Special Airport Oberpfaffenhofen. As given in Fig. 7(b), the data contain the typical scatterers such as the parking apron, runway, lawns, and facilities. Fig. 7(b) illustrates the developed classification, where the runway and parking apron are clearly discriminated from the in-between lawn (lawn1). These targets, however, are indiscriminately classified as Z_5 in Fig. 7(a). Then, we cannot tell their difference in H/α. Thus, the combination of ⊥ and ⊤ also behaves better than Z_5. All these reflect the better partition performance of the approach in medium-entropy state.

As for the low-entropy state, we have three zones Z_6, Z_7, and Z_8 in H/α but four classes ┘, —, │, and ∫ in the proposed approach. As displayed in Fig. 5(b), the four classes geometrically partition the state into four zones with clear borders in terms of the C_4^1 permutation of r_S, r_D, r_H, and r_V. Z_7 in H/α signifies the low-entropy dipole scattering [9], and it is divided into — and │ in the proposed approach to indicate the low-entropy horizontal and vertical dipole scatterings, respectively. Despite the theoretical significance, Z_7 is generally rare in the real PolSAR data because Cloude and Pottier [9] assigned it a very narrow area in the H/α space using the hard thresholds $\alpha = 42.5°$ and $\alpha = 47.5°$, as illustrated in Figs. 1(a) and 5(a). Fig. 6(a) reflects that only 0.15% of San Francisco data are classified to Z_7. The proposed approach improves this by using the adaptive ruling to enable a soft thresholding; — and │ then occupy a much wider zone that spans from about $\alpha = 25°$ to about $\alpha = 65°$, as exhibited in Fig. 5(b). From Fig. 6(d),

we observe that the majority of Z_7 is just situated in the area where — and | overlap with each other. The widening of — and |, on the other hand, implies the narrowing down of ⌟ and ∫ relative to Z_6 and Z_8, as shown in Fig. 5(a) and (b). Like ⌟, Z_6 also denotes the low-entropy dihedral scattering [9]; as listed in Table II, Z_6 comprises not only 99.09% of ⌟, but also 80.67% of —, while — reflects the dominant horizontal scattering instead of dihedral scattering. We can discriminate — from Z_6 by adding a boundary $\alpha = 65°$ to H/α. Likewise, both Z_8 and ∫ signify the low-entropy surface scattering, and almost all of ∫ (99.86%) are correctly mapped to Z_8, but Z_8 also covers 96.29% of |, as shown in Table II. Thus, Z_8 is divided into two parts in the proposed approach, as shown in Figs. 5(b) and 6(d). The black rectangle in Fig. 4(b) is a specific oceanic area of San Francisco. The angle α of this area (30.49°) is averagely much larger than the other oceanic area (5.50°) probably owing to the variation of the radar LOS [31]. (Based on the extended Bragg model, the influence of angle of incidence, roughness disturbance, and dielectric constant on the classification will be evaluated latter.) This difference in scattering is identified by the proposed approach and Wishart $SPAN/H/A/\alpha$ [31], but it is lost in H/α unless we add a new boundary $\alpha = 25°$. The adaptive approach thus performs better in the partitioning of the low-entropy state.

Cloude and Pottier [9] gave some qualitative elucidations on the physical scattering characteristics of Z_i in H/α, which have been investigated on many polarimetric radar data sets [26]–[31], but potential misleading is also inevitable. For example, both Z_2 and Z_4 are elucidated as vegetation scattering but with different scattering randomness [9]. This may mislead the inexperienced readers or users to identify scatterers that ascribed to Z_2 or Z_4 as vegetation, oppugn the results when Z_2 or Z_4 appears in the nonvegetation area [such as the beach area and SoMa[1] in Fig. 4(a)], and ignore the fact that scatterers that give vegetation scattering are not all vegetation scatterers. This obscurity is avoided in the proposed approach by relating Z_i to the canonical models, and a model-based understanding of H/α is thus enabled. Moreover, it is often difficult to demonstrate the physical characteristics of Z_1 and Z_2 on the real polarimetric radar data set because speckle and noise will result in biased parameter estimation, particular in the high-entropy environments [44]. As illustrated in Fig. 4(a) and (b), classes ☼ and ┼ in the proposed approach can achieve very consistent results as zones Z_1 and Z_2 in H/α. As also listed in Table II, 97.48% of ☼ and 89.18% of ┼ are registered into Z_1 and Z_2. Such consistency enables us to relate Z_2 to $\boldsymbol{T_{RAS}}$ and Z_1 to $\boldsymbol{T_{RIS}}$, which provides a novel understanding of Z_1 and Z_2. Cloude and Pottier [9] interpreted Z_2 as the scattering from a cloud of anisotropic needle-like particles. This elucidation just depicts how $\boldsymbol{T_{RAS}}$ is modeled by Freeman and Durden [12], and we can hence use $\boldsymbol{T_{RAS}}$ to characterize Z_2. Z_1 is identified as the multiple scattering of high entropy, and Cloude and Pottier [9] pointed out that it is still possible to distinguish double bounce mechanisms in Z_1. The consistency of 97.48% between ☼ and Z_1 suggests that $\boldsymbol{T_{RIS}}$ can model Z_1 perfectly. $\boldsymbol{T_{RIS}}$ signifies the random isotropic scattering, which, however, indicates that it is difficult to further distinguish scattering mechanisms in Z_1.

B. Comparison With the Chen Classification

The H/α classification begins with the assumption that there is always a dominant mean scattering $\boldsymbol{u}_0$ in each cell [9]. This is avoided in both Chen and the developed classifications in terms of the combination of major scattering and minor scattering. It should be noted that the major and minor scatterings are not the major and minor components of scattering $\boldsymbol{T}$ but the dominant and subdominant scattering mechanisms of $\boldsymbol{T}$. They provide an accurate description of scattering $\boldsymbol{T}$ from two different points of view and enable the proposed approach's nice discrimination, as demonstrated in Section V-A.

The Chen classification only uses the canonical single scatterings $\boldsymbol{T_S}$, $\boldsymbol{T_D}$, and $\boldsymbol{T_R}$ because Chen similarity measures the similarity between a mixed scattering and a canonical scattering [33]. $\boldsymbol{T_S}$, $\boldsymbol{T_D}$, and $\boldsymbol{T_R}$ are used to depict all the three states, and the states are delimited by the state boundaries $H = 0.36$ and $H = 0.855$. By analyzing the scatterings of San Francisco data, Chen *et al.* [35] developed a statistical method to determine the boundaries: the histogram of H is first achieved and filtered for a smoothed curve, and the inflection points of the curve are then located and identified as the boundaries on the H-axis. Nevertheless, potential nonrobustness arises when we use the method to the ESAR data of Oberpfaffenhofen. First, the result of the method is sensitive to the number of histogram bins and size of smoothing filtering used in the construction of the curve. Second, it is impossible to ensure that just two prominent inflection points (corresponding to the two H boundaries) are always located. Far more than two inflection points are identified although the curve is sufficiently smoothed, and we have no idea to make a selection among them. Hence, the statistical method fails on this data set. To make the Chen classification still available, we tried to adopt borders $H = 0.36$ and $H = 0.855$ obtained on San Francisco to Oberpfaffenhofen, but unacceptable classification is achieved. The blue triangle in Fig. 7(b) is a lawn (lawn2) that is relatively smoother ($0.36 < H < 0.5$) than lawn1 ($H > 0.5$). It is discriminable from lawn1 in Fig. 7(a) and (b) for $H = 0.5$ or its alternative $H_s = 0.31345$ is used as the state border of low entropy and medium entropy in H/α and the developed approach, but is

[1]SoMa denotes the South of Market. It is a dense urban area in San Francisco. Different from other region of San Francisco, streets here are neither horizontal nor vertical but are about 40° tilted [43]. Such planning leads to a misalignment (azimuth tilting) between the vertical wall of building and the azimuth direction of radar in view of the fact that building is generally constructed along the street. Then, the normal of wall will be no longer within the radar incidence plane, and target orientation is created. Moreover, azimuth tilting aggravates the scattering complexity and randomness, and leads H/α and the developed classification to attribute the majority of SoMa to the high-entropy classes Z_1 and Z_2 or ☼ and ┼. This cannot be compensated by any unitary deorientation method for entropies H and H_s that are roll-invariant, which will be presented in Section V-C. SoMa becomes a challenge for polarimetric processing procedures for its predominant volume/vegetation scattering comparable to that of vegetation. We can resort to mixed scattering models $\boldsymbol{T_{RIS}}$ and $\boldsymbol{T_{RAS}}$ to avoid the misinterpretation of SoMa as vegetation, but it is really difficult for us to further tell the difference between the high-entropy vegetation and azimuth-tilted buildings using the polarimetric data alone unless radar interferometry is incorporated for "entropy control" [3].

indiscriminable if $H = 0.36$ is used. The changing entropy statistics from data to data shows the data-dependent property of the Chen classification. The random similarity generalizes the Chen similarity to measure the similarity between two mixed scatterings, and nine models are used in the developed approach including five mixed canonical scatterings. Instead of describing scattering $\boldsymbol{T}$ with all the models, we adopt a correspondence principle by depicting $\boldsymbol{T}$ only with models of the same state. This enables us an adaptive determination of the state of $\boldsymbol{T}$ independent of a particular data, and a nice alternative to the state delimitation of H/α is obtained. Hence, we suggest using (9) or their H/α alternatives $H = 0.5$ and $H = 0.9$ as the state borders in the Chen classification. And the Chen classification of Oberpfaffenhofen in the following just uses this delimitation.

Figs. 4(c) and 7(c) illustrate the Chen classifications of San Francisco and Oberpfaffenhofen. These results are obtained on the original data set without deorientation as the Chen classification is susceptible to deorientation. Fig. 5(c) and the third row of Fig. 6 further display the H/α mapping and the α histogram of Fig. 4(c). Compared with that in H/α and in the proposed approach, the high-entropy state in the Chen classification is extended on the H-axis, as shown in Fig. 5(c). Nevertheless, it is intactly identified as class R in Fig. 6(i). Thus, the Chen classification cannot provide the equivalent performance as H/α and the proposed approach in discrimination of random anisotropic scattering and random isotropic scattering.

The state of medium entropy in Fig. 5(c) is also prolonged on the H-axis and is attributed into six classes, MSD, MSV, MDS, MDV, MVS, and MVD in terms of C_3^2 of $\boldsymbol{T_S}$, $\boldsymbol{T_D}$, and $\boldsymbol{T_R}$. However, the classes cannot geometrically align this state into three clear-cut zones such as Z_3, Z_4, and Z_5 in H/α and ⊤, ⊥, ⫡, ⫪, ⫫, and ⫯ in the developed approach. We can roughly find only two zones in Fig. 5(c), the upper zone MDS, MDV, MVS, and MVD, and the lower zone MSD and MSV. The upper zone corresponds to Z_3, and this indicates that Z_3 is classified into MDS, MDV, MVS, and MVD in the Chen classification, while Z_3 is attributed into ⫯, ⫪, ⫫, and ⫡ in the proposed approach. The percentage in Fig. 6 lists how many pixels of the scene of San Francisco are classified into a certain class. As listed in Fig. 6(h), MDS accounts for 22.72% but MVS, MDV, and MVD only take up 2.1%, while the percents for ⫯, ⫪, ⫫, and ⫡ are more harmonious, they are 5.18%, 7.54%, 3.53%, and 6.65%, respectively, as illustrated in Fig. 6(e). Thus, better urban discrimination is shown in Fig. 4(b) than in Fig. 4(c). The lower zone corresponds to Z_4 and Z_5 while Z_4 and Z_5 correspond to ⊤ and ⊥ in the proposed approach. As listed in Fig. 6, Z_4 and Z_5 account for 14.78% and 6.76% of the scene, while MSD and MSV take up 17.68% and 1.70%. The majority of Z_4 and Z_5 are classified as MSD, and MSV is only responsible for the minority. MSD and MSV thus cannot enable the equivalent discrimination as Z_4 and Z_5, although they can avoid the semantic obscure of Z_4 and Z_5. For instance, we can still identify airport facilities in Fig. 7(a), but such information is almost entirely lost in Fig. 7(c), let alone further identify runway and parking apron from lawn like ⊤ and ⊥ of the developed classification [Fig. 7(b)] do. All these show the better performance of $\boldsymbol{T_{RH}}$, $\boldsymbol{T_{RV}}$, and $\boldsymbol{T_{RD}}$ than $\boldsymbol{T_S}$, $\boldsymbol{T_D}$, and $\boldsymbol{T_R}$ in discrimination of scatterings of medium randomness.

The extension of the high- and medium-entropy states means the reduction of the low-entropy state on the H-axis compared with that in H/α and the proposed approach. LD, LV, and LS of the Chen classification divide the state of low entropy into two zones, as given in Fig. 5(c). LD and LV show the deoriented and oriented dihedral scatterings, and they are correctly aligned to Z_6 which reflects the low-entropy dihedral scattering. Nonetheless, as indicated in Fig. 6(g), LV accounts only 0.02% of San Francisco scene and is disabled after deorientation. Thus, the partition of Z_6 into LD and LV is somewhat insignificant. LS corresponds to Z_7 and Z_8, which signifies that we cannot extract dipole scattering from surface scattering in the Chen classification, let alone further divide it into the horizontal scattering — and vertical scattering | just as the proposed approach does. Thus, the Chen classification cannot provide nice discrimination of scatterings in low-entropy state.

C. Influence of Orientation

The influence of scattering orientation and the importance of deorientation operation have been presented in Section III-C. However, deorientation is unnecessary for H/α because H and α are invariant to the unitary roll transform $\boldsymbol{U_\varphi}$ [2], [9].

The entropy H_s in (7) can be further formulated as [36]

$$H_s = -\log_3\left(\frac{\mathrm{Tr}(\boldsymbol{T}\boldsymbol{T}^H)}{(\mathrm{Tr}(\boldsymbol{T}))^2}\right) = -\log_3\left(\frac{\sum_{i=1}^3 \lambda_i^2}{\left(\sum_{i=1}^3 \lambda_i\right)^2}\right). \quad (11)$$

Then, H_s relates only to the eigenvalues λ_i of $\boldsymbol{T}$, thus is also roll-invariant, and so is the partition of three states in the developed approach. The first row of Fig. 8 displays the angle α histogram of each class of the developed approach on the San Francisco scene with no deorientation, and the deoriented counterparts are given in the second row of Fig. 6. As expected, the three states take up 38.9%, 49.57%, and 11.53% of the scene whether we perform deorientation or not.

From the definition of random similarity in (3), one can easily obtain

$$r\left(\boldsymbol{U_\varphi}\boldsymbol{T}\boldsymbol{U_\varphi}^H, \boldsymbol{T_c}\right) = r\left(\boldsymbol{T}, \boldsymbol{U_\varphi}\boldsymbol{T_c}\boldsymbol{U_\varphi}^H\right) \neq r(\boldsymbol{T}, \boldsymbol{T_c}) \quad (12)$$

which indicates that the random similarity r is not roll-invariant, but we can obtain the deoriented r by just rotating the canonical model $\boldsymbol{T_c}$. Hence, the r-based determination of the 10 or 12 classes in the Chen classification or the developed approach is roll-dependent. Deorientation has to be conducted beforehand for the two classifications. The second row of Fig. 8 also shows the α histograms of the Chen classification on deoriented data with the oriented ones being given in the third row of Fig. 6. Despite the importance, deorientation will disenable classes LV, MSV, MVS, and MVD of the Chen classification, as shown in Fig. 8, because r_R will never exceed r_D after deorientation, as shown in the Appendix. Rather than improving the performance, deorientation

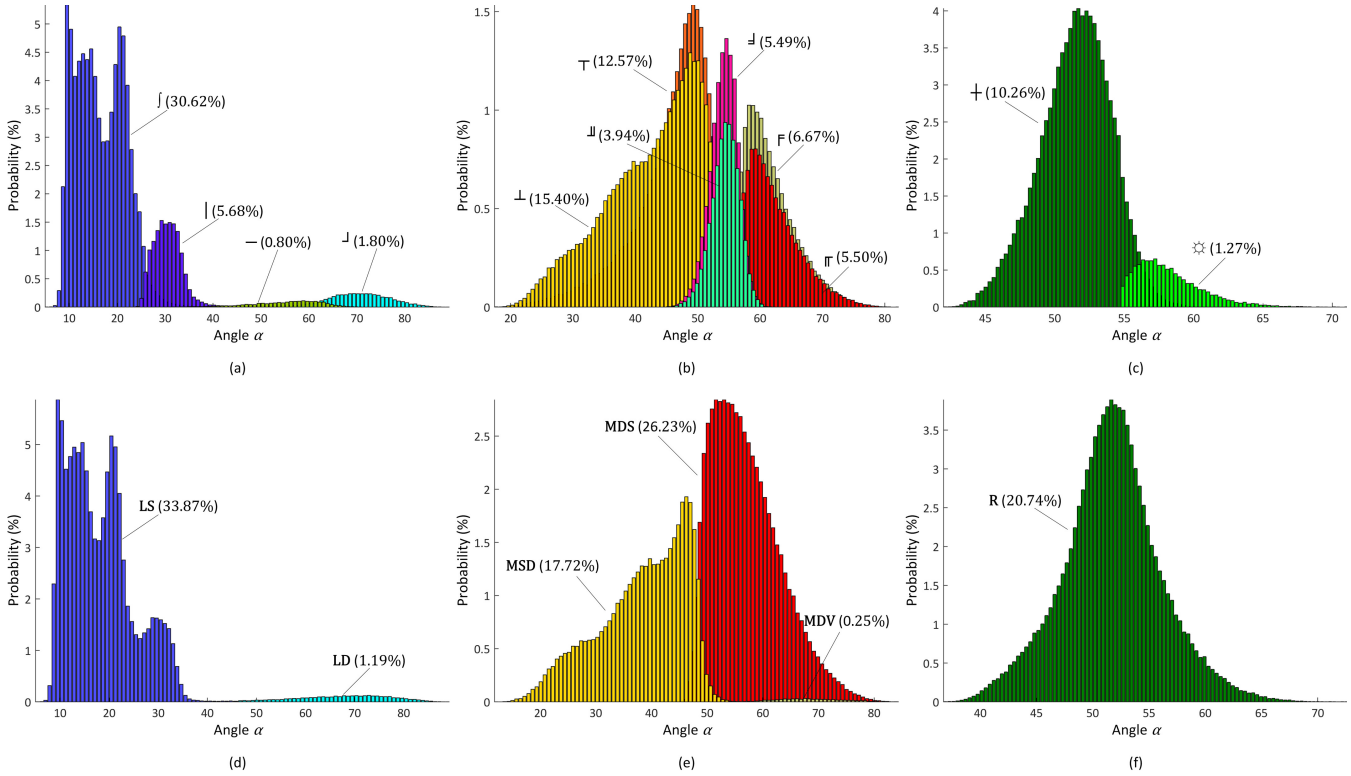

Fig. 8. Alpha angle histograms of (First row) adaptive classification (without deorientation) and (Second row) Chen classification (with deorientation) in (First column) low-entropy state, (Second column) medium-entropy state, and (Third column) high-entropy state on the AIRSAR San Francisco data to evaluate the influence of deorientation on the classifications. The percentage in the bracket summarizes how many pixels of the scene are attributed to a certain class.

degrades the Chen classification. Since model $\boldsymbol{T_R}$ is incompetent to describe the volume scattering and is also susceptible to deorientation, it is eliminated from the list of nine canonical models involved in the proposed classification. As formulated in the Appendix, T_{11} term and *SPAN* of $\boldsymbol{T}$ are roll-invariant; similarities r_S, r_{RAS}, and r_{RIS} are thus also independent of rotation, so are the high-entropy classes ☼ and ┼, as shown in Figs. 6(f) and 8(c). Similarity r_D becomes large after deorientation, as shown in (A6). As a result, ┘ increases from 1.8% to 1.93%, as displayed in Figs. 6(d) and 8(a). Then, the conservation of the state occurrence indicates the decrease of other classes. As shown, ∫ decreases from 30.62% to 30.53%, and the dipole scatterings | and — are reduced from 6.48% to 6.44%. The similar changes can also be found in Figs. 6(e) and 8(b). After deorientation, the dihedral scattering-related classes ┛, ┣, ╇, and ┳ increase from 21.6% to 22.9%, and the dipole scattering-related classes ┴ and ┬ change from 27.97% to 26.67%. Hence, deorientation does not disenable any class in the proposed approach, and the resulted changes are gentle. Fig. 7(d) shows the classification of Oberpfaffenhofen data with no deorientation. Comparing with its deoriented counterpart in Fig. 7(b), one can find tiny changes. A slightly clear change appears in the black rectangle of Fig. 7(b) which reflects some buildings. They are attributed as ┴ and ┬ and are indiscriminable from the surroundings in Fig. 7(d), but as ╇ in Fig. 7(b) which identifies not only the potential minor ground-wall dihedral scattering ┘ but also the major vertical wall scattering |.

D. Influence of Speckle Filtering

Like H/α, the developed classification also needs incoherent averaging of a number of neighboring pixels to avoid the biased classification. As for H/α, Lopez-Martinez *et al.* [44] and Lee *et al.* [45] have investigated the effects of speckle filtering on it and suggested using 7×7 (5×5) or larger averaging window for the estimation of H (α). Lee and Pottier [2] further indicated that the H estimation from RLF_7 performs even better than that from boxcar filter although RLF_7 cannot offer enough averages for reliable estimate. An evaluation of the effect of RLF_n on the proposed approach is simply given here. The first row of Fig. 9 shows the classifications of San Francisco when RLF_1 (with no filtering), RLF_3, RLF_5, and RLF_9 are used as filter, respectively (and deorientation should also be carried out after the filtering). The corresponding H/α classifications are also displayed in the second row of Fig. 9 for comparison, while the performance of the two classifications under RLF_7 has been displayed in Fig. 4. Although the data set has been averaged with 4×4 window in the estimation of coherency matrix, such filtering is insufficient for target classification, because classifications in Fig. 9(a) and (e) are still heavily speckled. This prevents us from bridging the classification to the ground truth. The classifications are greatly improved by simply averaging the data with RLF_3, RLF_5, RLF_7, or RLF_9. Such improvement is mainly attributed to the increase of scattering randomness. The green-coded Z_1 and ☼ as well as the dark green-coded Z_2 and ┼ become much clearer from RLF_3 to RLF_5, and further to RLF_7. This

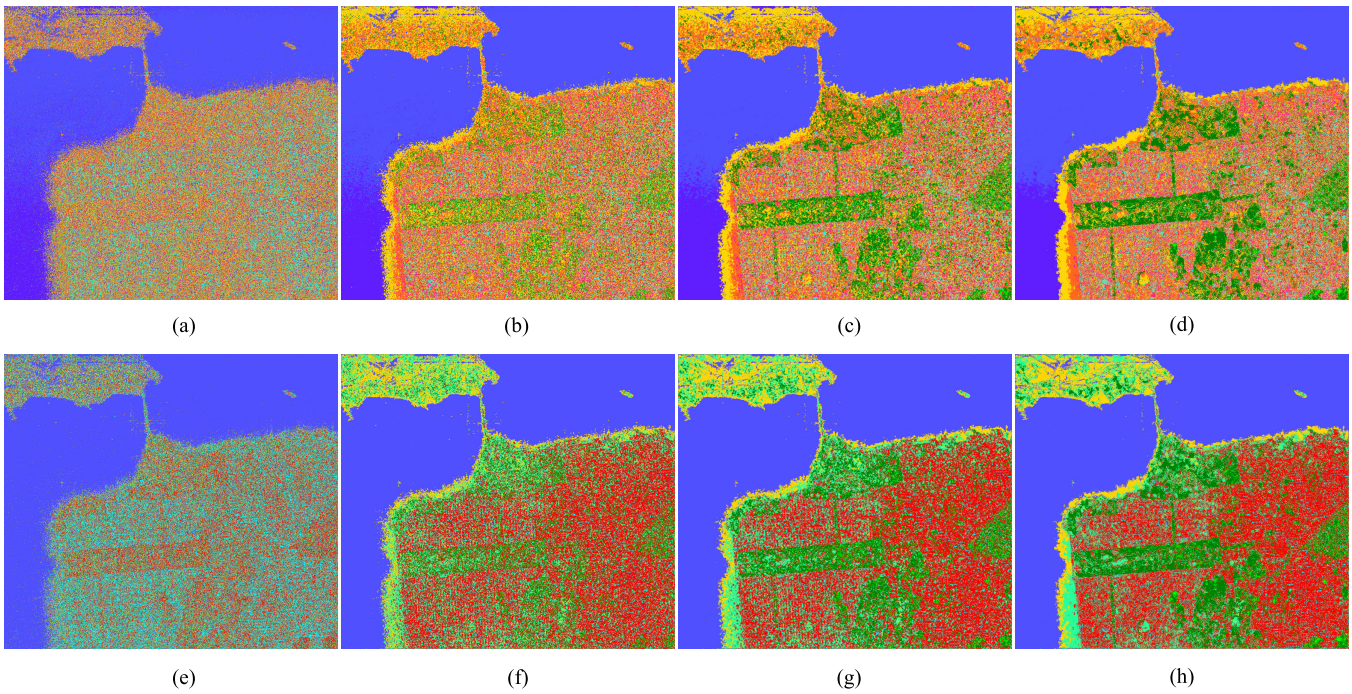

Fig. 9. Influence of refined Lee speckle filtering with (First column) 1×1 (i.e., without filtering), (Second column) 3×3, (Third column) 5×5, and (Fourth column) 9×9 large aligned windows on (First row) adaptive classification and on (Second row) H/α classification. It is shown that the influences of speckle filtering on the two classifications are comparable and consistent. The existing knowledge on the influence of filtering on H/α can be extended to the adaptive classification.

just indicates the increase of entropy, i.e., H_s increases with the increasing size of averaging. However, besides introducing the square imprint, the effects of filtering on the scattering similarity parameters listed in Table I are relatively limited. The similar finding on H and α has been presented in [44] and [45]. Therefore, the influences of speckle filtering on the proposed approach and on H/α are comparable and consistent. The existing knowledge on the influences of filtering on H/α can be extended to the proposed classification naturally. Larger window, of course, provides better estimation (although the changes from RLF_7 to RLF_9 are relatively small), but at the risk of degrading spatial resolution. RLF_7 is sufficient for the developed approach if we take the compromise between resolution and parameter estimation into consideration.

E. Influence of Incidence Angle

The polarimetric backscattering of a radar target with actual geometric and material parameters is sensitive to the incidence angle. As a result, the coherency matrix $\boldsymbol{T}$ is strongly dependent on the variation of incidence angle, so are the random similarity r and entropy H_s as well as the results of adaptive classification, although the involved canonical models in Table I are constant. Here, we simply adopt the randomly rough surface to exemplify the influence of incidence angle on the proposed approach. The small perturbation model (or Bragg model) fails to describe the cross-polarization and depolarization effects of random surface scattering [3]. To introduce roughness disturbance, the extended Bragg (X-Bragg) model is developed by randomly orienting the Bragg surface around LOS [29]. Then, the coherency matrix $\boldsymbol{T}_X$ of X-Bragg surface is of the following reflection symmetry [29]:

$$\boldsymbol{T}_X = \begin{bmatrix} a & b\mathrm{sinc}(2\Delta) & 0 \\ b^*\mathrm{sinc}(2\Delta) & c(1+\mathrm{sinc}(4\Delta)) & 0 \\ 0 & 0 & c(1-\mathrm{sinc}(4\Delta)) \end{bmatrix} \tag{13}$$

where sinc $(\cdot)$ is the Sinc function; $\Delta \in [0, 90°]$ shows the width of the random distribution of local orientation which models the amount of roughness disturbance [29]. Coefficients a, b, and c are given by the Bragg scattering matrix elements R_{HH} and R_{VV}

$$\begin{cases} a = |R_{\mathrm{HH}} + R_{\mathrm{VV}}|^2 \\ b = (R_{\mathrm{HH}} + R_{\mathrm{VV}})(R_{\mathrm{HH}} - R_{\mathrm{VV}})^* \\ c = \dfrac{1}{2}|R_{\mathrm{HH}} - R_{\mathrm{VV}}|^2 \end{cases} \tag{14}$$

with

$$\begin{cases} R_{\mathrm{HH}} = \dfrac{\cos\theta - \sqrt{\varepsilon - \sin^2\theta}}{\cos\theta + \sqrt{\varepsilon - \sin^2\theta}} \\ R_{\mathrm{VV}} = \dfrac{(\varepsilon - 1)(\sin^2\theta - \varepsilon(1 + \sin^2\theta))}{(\varepsilon\cos\theta + \sqrt{\varepsilon - \sin^2\theta})^2} \end{cases} \tag{15}$$

where θ is the angle of incidence and ε is the dielectric constant which is closely related to the volumetric soil moisture content [46]. Combine (6), (7), and (13), the entropy H_s of $\boldsymbol{T}_X$ (i.e., H_{sX}) is then formulated as

$$H_{sX} = -\log_3\left(\frac{a^2 + 2c^2(1 + \mathrm{sinc}^2(4\Delta)) + 2|b|^2\mathrm{sinc}^2(2\Delta)}{(a + 2c)^2}\right). \tag{16}$$

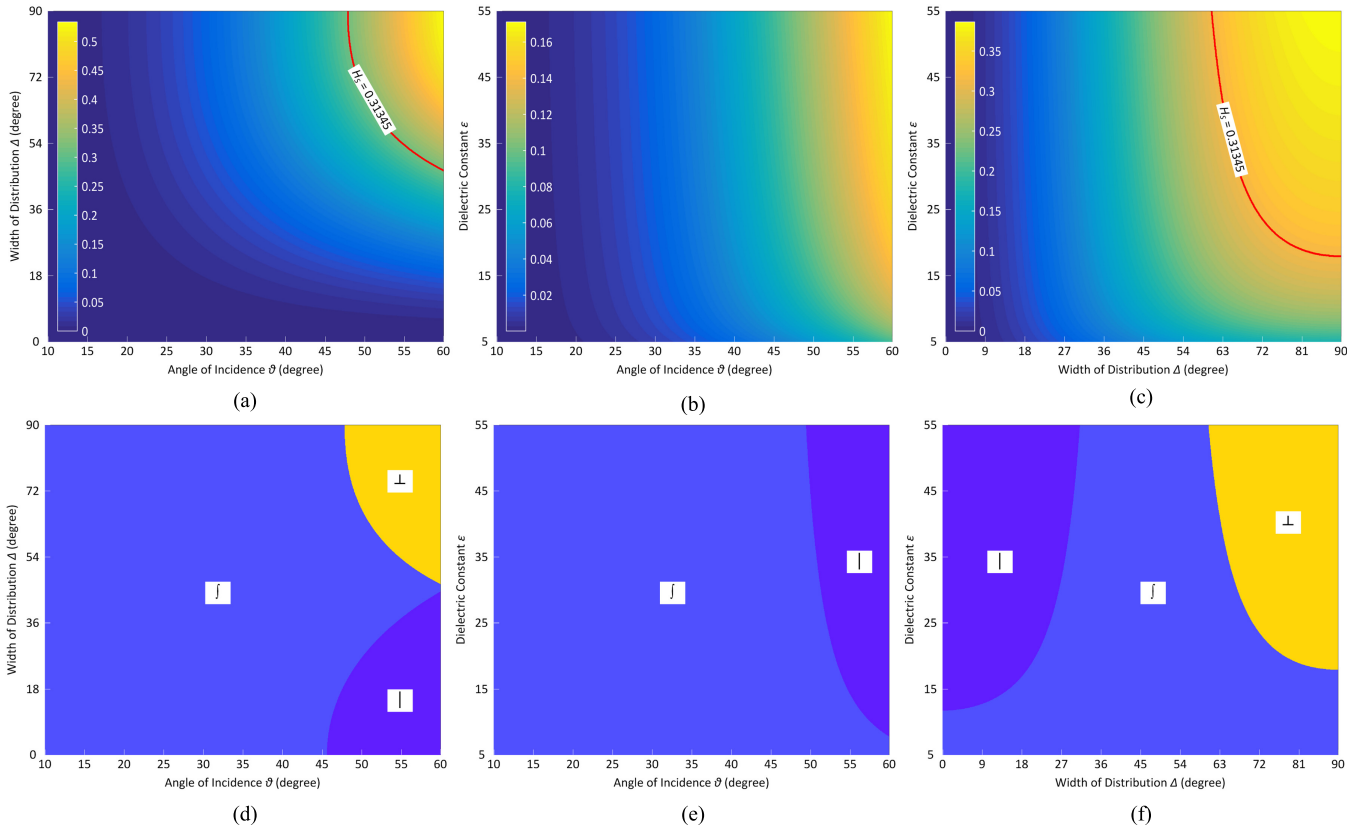

Fig. 10. Influence of the angle of incidence θ, width of distribution Δ, and dielectric constant ε of X-Bragg surface on (First row) entropy H_s and on (Second row) adaptive classification. As shown, H_s and the classification result are influenced by θ, Δ, and ε. For convenience, we denote them as $H_{sX}(\theta, \Delta, \varepsilon)$ and $C(\theta, \Delta, \varepsilon)$, respectively. The output of C is an RGB color displayed in Fig. 1(b) which corresponds to one of the 12 classes. (a)–(c) Images of $H_{sX}(\theta, \Delta, 30)$, $H_{sX}(\theta, 30°, \varepsilon)$, and $H_{sX}(50°, \Delta, \varepsilon)$, respectively. (d)–(f) Results of $C(\theta, \Delta, 30)$, $C(\theta, 30°, \varepsilon)$, and $C(50°, \Delta, \varepsilon)$, respectively.

H_{sX} depends on the three factors θ, Δ, and ε, and is denoted as a function $H_{sX}(\theta, \Delta, \varepsilon)$. To qualitatively investigate the influence, Fig. 10(a)–(c) shows the images of $H_{sX}(\theta, \Delta, 30)$, $H_{sX}(\theta, 30°, \varepsilon)$, and $H_{sX}(50°, \Delta, \varepsilon)$, respectively. It is shown that H_{sX} increases with the increase of θ, Δ, and ε. When incidence angle θ is low, H_{sX} almost has no change with the increase of Δ and ε but stays in a very low state, and so is the case of low roughness surface (i.e., Δ is small). However, this does not hold for the case of low dielectric constant ε. Compared with θ and Δ, ε imposes gentle influence on H_{sX}. H_{sX} bears much more sensitive to the change of θ and/or Δ, particularly when θ or Δ is high. It oversteps the border $H_s = 0.31345$ in Fig. 10(a) and (c), and shows the state transition from low entropy to medium entropy. Such transition does not arise in Fig. 10(b) because the surface here is relatively smooth with $\Delta = 30°$. But H_s in any case does not overstep the border $H_s = 0.82935$ between the states of medium and high entropy, i.e., high-entropy surface scattering does not exist. This finding is consistent with H/α and the proposed classification.

The impacts of θ, Δ, and ε on the similarity parameters listed in Table I are complex: the constant r_{RIS} is independent of θ, Δ, and ε; r_S and r_{RAS} are only independent of Δ[2]; while the rest are dependent on all. Instead of evaluating the influence on each r, here, we directly investigate the influences of θ, Δ, and ε on the final classification. We also denote this as a function $C(\theta, \Delta, \varepsilon)$, where the output of C is an RGB color defined in Fig. 1(b) which corresponds to one of the 12 classes. Fig. 10(d)–(f) displays $C(\theta, \Delta, 30)$, $C(\theta, 30°, \varepsilon)$, and $C(50°, \Delta, \varepsilon)$, respectively. Three surface-related classes $|$, $\int$, and $\perp$ are correctly identified by the approach: $|$ and $\int$ represent two different kinds of low-entropy surface scatterings, while $\perp$ shows the medium-entropy surface scattering. The identification of $\perp$ only depends on H_{sX} since $\perp$ in Fig. 10(d) and (f) just corresponds to the high-entropy area in Fig. 10(a) and (c), while the discrimination of $|$ from $\int$ in low entropy is determined by the similarities r. Both classes $|$ and $\int$ can be observed from Fig. 10(d)–(f). Thus, the determination of scattering mechanism is also influenced by all the parameters θ, Δ, and ε. These just exemplify a physical reality of polarimetric radar targets: the polarimetric classification result of the targets is determined not only by the targets themselves, but also by the observation geometry of radar. This should be kept in our mind when we use the classification for any advanced application.

VI. Discussion

Characterizing the complex scattering using the combination of canonical models is a promising method to the PolSAR data

[2]Therefore, r_S and r_{RAS} enable a separation of roughness and moisture effect. Nonetheless, only r_S may be useful for soil moisture estimation [29], in view of the fact that high-entropy surface does not exist.

classification. Unlike the model-based target decompositions in which the canonical models are serially applied to pursuing the components of the complex scattering, the canonical models in the proposed approach are used parallel to pursue the scattering mechanism of the complex scattering. Hence, instead of solving the balance equations for the scattering power of each canonical model, the contribution of each canonical model is determined by the simple similarity measurement in the proposed approach. This presumes a flexible scattering characterization and allows us to try different canonical models parallelly. For example, all the three models $\boldsymbol{T_{RH}}$, $\boldsymbol{T_{RV}}$, and $\boldsymbol{T_{RD}}$ are utilized to characterize the scattering mechanism of a medium-entropy scattering in the proposed classification, but only one of them is identified when decomposing a scattering because only one volume component is allowed in the extended four-component decomposition [14]. Thus, the canonical scattering models in the proposed approach are not competitive but cooperative. They together provide us a good characterization of the complex scattering.

The eigenvector-based decomposition and the model-based decomposition constitute two main branches of the polarimetric target decomposition approaches [2]. As a hybrid, the developed approach adopts the canonical scattering models widely used in the model-based decomposition to obtain a target classification consistent with H/α, and provides us a novel improvement and understanding of H/α from the model-based point of view. The correspondence principle is employed to adaptively identify the models in terms of entropy matching, which may be also useful in model-based decompositions for parallel model selection.

By incorporating the 12 classes into the techniques such as fuzzy clustering [47], neural network [48], and fuzzy neural network [49] by virtue of the complex Wishart distribution [50], the proposed approach can be used for unsupervised terrain and land-use classification. The application to physical information (such as soil moisture) retrieval will be conducted in the future. The nice performance of the approach has also been checked on other PolSAR data sets with a different frequency and resolution.

VII. Conclusion

The eigenvector-based and model-based decompositions are not independent of each other but can be integrated to enable an adaptive classification of PolSAR images. Random similarity is a useful tool for the parallel analysis of the complex scatterings. The scattering similarity-based Chen classification is susceptible to deorientation operation, and cannot enable the equivalent discrimination as H/α although it can solve certain obscures in H/α. The correspondence principle-based adaptive selection of the canonical models enables a data-independent determination of the scattering randomness states and a competent alternative to the Cloude–Pottier deciding of the states, which validates that the H borders in H/α are not dependent on a particular data set. Entropy H_s is a nice alternative to Cloude–Pottier entropy H for scattering randomness depiction. Unlike the model-based target decompositions, the canonical models are parallelly permutated and combined in the classification to achieve a fine depiction of the scattering mechanism based on the scattering similarity, and the assumption in H/α that there is always a dominant average scattering in each cell is also avoided. The classification covers 12 classes with each one carrying a unique symbol to reveal a specific scattering. It does not depend on a particular data set, provides a model-based improvement of H/α, avoids the hard thresholding and semantic obscures in H/α, and presents better target discrimination than H/α and Chen classification.

Appendix A

The deoriented coherency $\boldsymbol{T}'$ is expressed as

$$\boldsymbol{T}' = \boldsymbol{U_\varphi} \boldsymbol{T} \boldsymbol{U_\varphi^{\mathrm{H}}}, \boldsymbol{U_\varphi} = \begin{bmatrix} 1 & 0 & 0 \\ 0 & \cos 2\varphi & \sin 2\varphi \\ 0 & -\sin 2\varphi & \cos 2\varphi \end{bmatrix} \tag{A1}$$

where $\boldsymbol{U_\varphi}$ denotes the unitary roll transform. Bring (1) into (A1)

$$\begin{cases} T_{11} = T'_{11} \\ T'_{22} = T_{22}\cos^2 2\varphi + \mathrm{Re}(T_{23})\sin 4\varphi + T_{33}\sin^2 2\varphi \\ T'_{33} = T_{22}\sin^2 2\varphi - \mathrm{Re}(T_{23})\sin 4\varphi + T_{33}\cos^2 2\varphi. \end{cases} \tag{A2}$$

The rotation φ is obtained by minimizing T'_{33} term [39]–[41]

$$\frac{\partial T'_{33}}{\partial \varphi} = 0 \Rightarrow \tan 4\varphi = \frac{2\mathrm{Re}\,(T_{23})}{T_{22} - T_{33}}. \tag{A3}$$

Hence,

$$\begin{cases} \sin 4\varphi = \dfrac{2\mathrm{Re}(T_{23})}{\sqrt{(T_{22} - T_{33})^2 + 4(\mathrm{Re}(T_{23}))^2}} \\ \cos 4\varphi = \dfrac{T_{22} - T_{33}}{\sqrt{(T_{22} - T_{33})^2 + 4(\mathrm{Re}(T_{23}))^2}}. \end{cases} \tag{A4}$$

Combine (A2) and (A4), we have

$$\begin{aligned} T'_{22} - T'_{33} &= (T_{22} - T_{33})\cos 4\varphi + 2\mathrm{Re}(T_{23})\sin 4\varphi \\ &= \sqrt{(T_{22} - T_{33})^2 + 4(\mathrm{Re}(T_{23}))^2} \geq 0. \end{aligned} \tag{A5}$$

The deoriented similarity parameters r'_S, r'_D, and r'_R are defined

$$\begin{cases} r'_S = r(\boldsymbol{T}', \boldsymbol{T_S}) = \dfrac{T'_{11}}{T'_{11} + T'_{22} + T'_{33}} \\ \quad = \dfrac{T_{11}}{T_{11} + T_{22} + T_{33}} = r_S \\ r'_D = r(\boldsymbol{T}', \boldsymbol{T_D}) = \dfrac{T'_{22}}{T'_{11} + T'_{22} + T'_{33}} \\ \quad = \dfrac{T'_{22}}{T_{11} + T_{22} + T_{33}} \geq r_D \\ r'_R = r(\boldsymbol{T}', \boldsymbol{T_R}) = \dfrac{T'_{33}}{T'_{11} + T'_{22} + T'_{33}} \\ \quad = \dfrac{T'_{33}}{T_{11} + T_{22} + T_{33}} \leq r_R. \end{cases} \tag{A6}$$

Then, (A5) indicates that

$$r'_D \geq r'_R. \tag{A7}$$

Therefore, four of the ten classes in the Chen classification, i.e., LV, MSV, MVS, and MVD, will be disenabled after deorientation.

ACKNOWLEDGMENT

The authors would like to thank the National Aeronautics and Space Administration/Jet Propulsion Laboratory, Pasadena, CA, USA, and the German Aerospace Center, Oberpfaffenhofen, Germany, for providing the PolSAR data sets. They would also like to thank the anonymous reviewers for their valuable comments and suggestions.

REFERENCES

[1] W.-M. Boerner, *Direct and Inverse Methods in Radar Polarimetry*. Dordrecht, The Netherlands: Kluwer, 1992.

[2] J.-S. Lee and E. Pottier, *Polarimetric Radar Imaging: From Basics to Applications*. Boca Raton, FL, USA: CRC Press, 2009.

[3] S. R. Cloude, *Polarisation Applications in Remote Sensing*. Oxford, U.K.: Oxford Univ. Press, 2010.

[4] J. J. van Zyl and Y. Kim, *Synthetic Aperture Radar Polarimetry*. Hoboken, NJ, USA: Wiley, 2011.

[5] J. R. Huynen, "Phenomenological theory of radar targets," Ph.D. dissertation, Dept. Elect. Eng., Math. Comput. Sci., Tech. Univ. Delft, Delft, The Netherlands, 1970.

[6] W. A. Holm and R. M. Barnes, "On radar polarization mixed target state decomposition techniques," in *Proc. IEEE Nat. Radar Conf.*, Ann Arbor, MI, USA, Apr. 1988, pp. 249–254.

[7] J. Yang, Y.-N. Peng, Y. Yamaguchi, and H. Yamada, "On Huynen's decomposition of a Kennaugh matrix," *IEEE Geosci. Remote Sens. Lett.*, vol. 3, no. 3, pp. 369–372, Jul. 2006.

[8] D. Li and Y. Zhang, "Unified Huynen phenomenological decomposition of radar targets and its classification applications," *IEEE Trans. Geosci. Remote Sens.*, vol. 54, no. 2, pp. 723–743, Feb. 2016.

[9] S. R. Cloude and E. Pottier, "An entropy based classification scheme for land applications of polarimetric SAR," *IEEE Trans. Geosci. Remote Sens.*, vol. 35, no. 1, pp. 68–78, Jan. 1997.

[10] S. R. Cloude, "Uniqueness of target decomposition theorems in radar polarimetry," in *Direct and Inverse Methods in Radar Polarimetry*, vol. 1, W.-M. Boerner, Ed. Dordrecht, The Netherlands: Kluwer, 1992, pp. 267–296.

[11] R. Paladini, L. F. Famil, E. Pottier, M. Martorella, F. Berizzi, and E. D. Mese, "Lossless and sufficient Ψ-invariant decomposition of random reciprocal target," *IEEE Trans. Geosci. Remote Sens.*, vol. 50, no. 9, pp. 3487–3501, Sep. 2012.

[12] A. Freeman and S. L. Durden, "A three-component scattering model for polarimetric SAR data," *IEEE Trans. Geosci. Remote Sens.*, vol. 36, no. 3, pp. 963–973, May 1998.

[13] Y. Yamaguchi, T. Moriyama, M. Ishido, and H. Yamada, "Four-component scattering model for polarimetric SAR image decomposition," *IEEE Trans. Geosci. Remote Sens.*, vol. 43, no. 8, pp. 1699–1706, Aug. 2005.

[14] A. Sato, Y. Yamaguchi, G. Singh, and S.-E. Park, "Four-component scattering power decomposition with extended volume scattering model," *IEEE Geosci. Remote Sens. Lett.*, vol. 9, no. 2, pp. 166–170, Mar. 2012.

[15] G. Singh, Y. Yamaguchi, and S.-E. Park, "General four-component scattering power decomposition with unitary transformation of coherency matrix," *IEEE Trans. Geosci. Remote Sens.*, vol. 51, no. 5, pp. 3014–3022, May 2013.

[16] W. An, Y. Cui, and J. Yang, "Three-component model-based decomposition for polarimetric SAR data," *IEEE Trans. Geosci. Remote Sens.*, vol. 48, no. 6, pp. 2732–2739, Jun. 2010.

[17] J. J. van Zyl, M. Arii, and Y. Kim, "Model-based decomposition of polarimetric SAR covariance matrices constrained for nonnegative eigenvalues," *IEEE Trans. Geosci. Remote Sens.*, vol. 49, no. 9, pp. 3452–3459, Sep. 2011.

[18] S. W. Chen, X. S. Wang, S. P. Xiao, and M. Sato, "General polarimetric model-based decomposition for coherency matrix," *IEEE Trans. Geosci. Remote Sens.*, vol. 52, no. 3, pp. 1843–1855, Mar. 2014.

[19] Y. Cui, Y. Yamaguchi, J. Yang, H. Kobayashi, S.-E. Park, and G. Singh, "On complete model-based decomposition of polarimetric SAR coherency matrix data," *IEEE Trans. Geosci. Remote Sens.*, vol. 52, no. 4, pp. 1991–2001, Apr. 2014.

[20] J. S. Lee, T. L. Ainsworth, and Y. Wang, "Generalized polarimetric model-based decompositions using incoherent scattering models," *IEEE Trans. Geosci. Remote Sens.*, vol. 52, no. 5, pp. 2474–2491, May 2014.

[21] E. Krogager, "New decomposition of the radar target scattering matrix," *Electron. Lett.*, vol. 26, no. 18, pp. 1525–1527, Aug. 1990.

[22] W. L. Cameron, N. N. Youssef, and L. K. Leung, "Simulated polarimetric signatures of primitive geometrical shapes," *IEEE Trans. Geosci. Remote Sens.*, vol. 34, no. 3, pp. 793–803, May 1996.

[23] R. Touzi, "Target scattering decomposition in terms of roll-invariant target parameters," *IEEE Trans. Geosci. Remote Sens.*, vol. 45, no. 1, pp. 73–84, Jan. 2007.

[24] S. R. Cloude and E. Pottier, "A review of target decomposition theorems in radar polarimetry," *IEEE Trans. Geosci. Remote Sens.*, vol. 34, no. 2, pp. 498–518, Mar. 1996.

[25] J.-S. Lee, M. R. Grunes, E. Pottier, and L. Ferro-Famil, "Unsupervised terrain classification preserving polarimetric scattering characteristics," *IEEE Trans. Geosci. Remote Sens.*, vol. 42, no. 4, pp. 722–731, Apr. 2004.

[26] L. Ferro-Famil, E. Pottier, and J.-S. Lee, "Unsupervised classification of multifrequency and fully polarimetric SAR images based on the H/A/Alpha-Wishart classifier," *IEEE Trans. Geosci. Remote Sens.*, vol. 39, no. 11, pp. 2332–2342, Nov. 2001.

[27] S. R. Cloude, J. Fortuny, J. M. Lopez-Sanchez, and A. J. Sieber, "Wide-band polarimetric radar inversion studies for vegetation layers," *IEEE Trans. Geosci. Remote Sens.*, vol. 37, no. 5, pp. 2430–2441, Sep. 1999.

[28] Y.-Q. Jin and F. Chen, "Polarimetric scattering indexes and information entropy of the SAR imagery for surface monitoring," *IEEE Trans. Geosci. Remote Sens.*, vol. 40, no. 11, pp. 2502–2506, Nov. 2002.

[29] I. Hajnsek, E. Pottier, and S. R. Cloude, "Inversion of surface parameters from polarimetric SAR," *IEEE Trans. Geosci. Remote Sens.*, vol. 41, no. 4, pp. 727–744, Apr. 2003.

[30] S. E. Park and W. M. Moon, "Unsupervised classification of scattering mechanisms in polarimetric SAR data using fuzzy logic in entropy and alpha plane," *IEEE Trans. Geosci. Remote Sens.*, vol. 45, no. 8, pp. 2652–2664, Aug. 2007.

[31] F. Cao, W. Hong, Y. Wu, and E. Pottier, "An unsupervised segmentation with an adaptive number of clusters using the $SPAN/H/\alpha/A$ space and the complex wishart clustering for fully polarimetric SAR data analysis," *IEEE Trans. Geosci. Remote Sens.*, vol. 45, no. 11, pp. 3454–3467, Nov. 2007.

[32] J. Yang, Y.-N. Peng, and S.-M. Lin, "Similarity between two scattering matrices," *Electron. Lett.*, vol. 37, no. 3, pp. 193–194, Feb. 2001.

[33] Q. Chen, Y. M. Jiang, L. J. Zhao, and G. Y. Kuang, "Polarimetric scattering similarity between a random scatterer and a canonical scatterer," *IEEE Geosci. Remote Sens. Lett.*, vol. 7, no. 4, pp. 866–869, Oct. 2010.

[34] D. Li and Y. Zhang, "Random similarity between two mixed scatterers," *IEEE Geosci. Remote Sens. Lett.*, vol. 12, no. 12, pp. 2468–2472, Dec. 2015.

[35] Q. Chen, G. Kuang, J. Li, L. Sui, and D. Li, "Unsupervised land cover/land use classification using PolSAR imagery based on scattering similarity," *IEEE Trans. Geosci. Remote Sens.*, vol. 51, no. 3, pp. 1817–1825, Mar. 2013.

[36] D. Li and Y. Zhang, "Random similarity-based entropy/alpha classification of PolSAR data," *IEEE J. Sel. Topics Appl. Earth Observ. Remote Sens.*, vol. 10, no. 12, pp. 5712–5723, Dec. 2017.

[37] J. R. Huynen, "Physical reality of radar targets," *Proc. SPIE*, vol. 1748, pp. 86–96, Feb. 1993.

[38] F. Xu and Y.-Q. Jin, "Deorientation theory of polarimetric scattering targets and application to terrain surface classification," *IEEE Trans. Geosci. Remote Sens.*, vol. 43, no. 10, pp. 2351–2364, Oct. 2005.

[39] J.-S. Lee and T. L. Ainsworth, "The effect of orientation angle compensation on coherency matrix and polarimetric target decompositions," *IEEE Trans. Geosci. Remote Sens.*, vol. 49, no. 1, pp. 53–64, Jan. 2011.

[40] Y. Yamaguchi, A. Sato, W.-M. Boerner, R. Sato, and H. Yamada, "Four-component scattering power decomposition with rotation of coherency matrix," *IEEE Trans. Geosci. Remote Sens.*, vol. 49, no. 6, pp. 2251–2258, Jun. 2011.

[41] W. An, C. Xie, X. Yuan, Y. Cui, and J. Yang, "Four-component decomposition of polarimetric SAR images with deorientation," *IEEE Geosci. Remote Sens. Lett.*, vol. 8, no. 6, pp. 1090–1094, Nov. 2011.

[42] G. Ropars, G. Gorre, A. Le Floch, J. Enoch, and V. Lakshminarayanan, "A depolarizer as a possible precise sunstone for Viking navigation by polarized skylight," *Proc. R. Soc. Lond. A, Math. Phys. Sci.*, vol. 468, no. 2139, pp. 671–684, Mar. 2012.

[43] E. C. Koeniguer, F. Weissgerber, N. Trouve, and J.-M. Nicolas, "A new light on origins of polarimetric misclassification of the SoMa district, due to the difficulty to predict entropy," in *Proc. POLINSAR*, Frascati, Italy, 2015, pp. 1–5.

[44] C. Lopez-Martinez, E. Pottier, and S. R. Cloude, "Statistical assessment of eigenvector-based target decomposition theorems in radar polarimetry," *IEEE Trans. Geosci. Remote Sens.*, vol. 43, no. 9, pp. 2058–2074, Sep. 2005.

[45] J. S. Lee, T. L. Ainsworth, J. P. Kelly, and C. Lopez-Martinez, "Evaluation and bias removal of multilook effect on entropy/alpha/anisotropy in polarimetric SAR decomposition," *IEEE Trans. Geosci. Remote Sens.*, vol. 46, no. 10, pp. 3039–3052, Oct. 2008.

[46] G. C. Topp, J. L. Davis, and A. P. Annan, "Electromagnetic determination of soil water content: Measurements in coaxial transmission lines," *Water Resour. Res.*, vol. 16, no. 3, pp. 574–582, Jun. 1980.

[47] L.-J. Du and J.-S. Lee, "Fuzzy classification of earth terrain covers using multi-look polarimetric SAR image data," *Int. J. Remote Sens.*, vol. 17, no. 4, pp. 809–826, 1996.

[48] K. S. Chen, W. P. Huang, D. H. Tsay, and F. Amar, "Classification of multifrequency polarimetric SAR imagery using a dynamic learning neural network," *IEEE Trans. Geosci. Remote Sens.*, vol. 34, no. 3, pp. 814–820, May 1996.

[49] C.-T. Chen, K.-S. Chen, and J.-S. Lee, "The use of fully polarimetric information for the fuzzy neural classification of SAR images," *IEEE Trans. Geosci. Remote Sens.*, vol. 41, no. 9, pp. 2089–2100, Sep. 2003.

[50] J.-S. Lee, M. R. Grunes, T. L. Ainsworth, L.-J. Du, D. L. Schuler, and S. R. Cloude, "Unsupervised classification using polarimetric decomposition and the complex Wishart classifier," *IEEE Trans. Geosci. Remote Sens.*, vol. 37, no. 5, pp. 2249–2258, Sep. 1999.

Dong Li (S'11–M'14) received the B.S. degree in electronic engineering from Xidian University, Xi'an, China, in 2008, and the Ph.D. degree in electrical engineering from the University of Chinese Academy of Sciences, Beijing, China, in 2013.

He is currently an Associate Professor with the Key Laboratory of Microwave Remote Sensing, National Space Science Center, Chinese Academy of Sciences, Beijing. His research interests include synthetic aperture radar (SAR) polarimetry, polarimetric target decomposition, polarimetric scattering modeling, SAR image registration, and computer SAR vision.

Dr. Li is a member of the Youth Innovation Promotion Association, Chinese Academy of Sciences. He received the President Scholarship for Outstanding Students of the Chinese Academy of Sciences in 2013 for his Ph.D. dissertation on the stereo processing and polarimetric analysis of SAR images.

Yunhua Zhang (M'00) received the B.S. degree in electrical engineering from Xidian University, Xi'an, China, in 1989, and the M.S. and Ph.D. degrees in electrical engineering from Zhejiang University, Hangzhou, China, in 1993 and 1995, respectively.

He is currently a Professor with the National Space Science Center, Chinese Academy of Sciences, Beijing, China, and also the Deputy Director of the Key Laboratory of Microwave Remote Sensing. He is also a Professor with the School of Electronic, Electrical and Communication Engineering, University of Chinese Academy of Sciences, Beijing, where he lectured modern radar theory and technology to the postgraduate students. His research interests include the system design and signal processing of microwave sensors (high-resolution radar, interferometric radar, radar altimeter, and noise radar), polarimetric radar target decomposition, application of compressive sensing in radar, and antennas and computational electromagnetics.

Dr. Zhang is the Chief Designer for the Chinese Tiangong-2 Interferometric Imaging Altimeter, which is the first spaceborne wide-swath radar altimeter launched in September 15, 2016.